

Fluctuation-induced higher-derivative couplings and infrared dynamics of the Quark-Meson-Diquark Model

Niklas Cichutek,^{1,*} Florian Divotgey,^{1,†} and Jürgen Eser^{1,‡}

¹*Institut für Theoretische Physik, Johann Wolfgang Goethe-Universität,
Max-von-Laue-Straße 1, D-60438 Frankfurt am Main, Germany*

(Dated: June 23, 2020)

In a qualitative study, the low-energy properties of the SO(6)-symmetric Quark-Meson-Diquark Model as an effective model for two-color Quantum Chromodynamics are investigated within the Functional Renormalization Group (FRG) approach. In particular, we compute the infrared scaling behavior of fluctuation-induced higher-derivative couplings of the linear Quark-Meson-Diquark Model and map the resulting renormalized effective action onto its nonlinear counterpart. The higher-derivative couplings of the nonlinear model, which we identify as the low-energy couplings of the Quark-Meson-Diquark Model, are therefore entirely determined by the FRG flow of their linear equivalents. This grants full access to their scaling behavior and provides insights into conceptual aspects of purely bosonic effective models, as they are treated within the FRG. In this way, the presented work is understood as an immediate extension of our recent advances in the SO(4)-symmetric Quark-Meson Model beyond common FRG approximations.

I. INTRODUCTION

In a series of recent publications [1–3], we presented a low-energy analysis of the (two-flavor) Quark-Meson Model (QMM), which was treated as a (linear) effective model of the fundamental theory of the strong interaction, Quantum Chromodynamics (QCD). To be precise, we expanded the effective action of the QMM up to (and including) fourth order in its bosonic field variables as well as their respective space-time derivatives. We applied the Functional Renormalization Group (FRG) approach [4–11] in order to (qualitatively) determine the scaling behavior of all higher-derivative couplings within the aforementioned derivative expansion, the latter of which substantially exceeds commonly used truncation schemes. As a result of this analysis, the low-energy limit of the QMM naturally emerges from the FRG integration of quantum fluctuations by transforming the linear realization of the SO(4)-symmetry (among the bosonic fields) into its nonlinear counterpart [2, 12–18]. According to the given expansion, the nonlinear realization encodes a complete set of (mostly momentum-dependent) pion self-interactions and thus defines the low-energy couplings of the model. Such calculations including higher-derivative interactions are generally very valuable as an (additional) consistency criterion for effective models.

An important consequence of the mapping between the (linear) QMM and its (nonlinear) low-energy limit is given by the fact that the low-energy couplings of the model are obtained as functions of the linear higher-derivative couplings. This provides access to their scaling behavior, which yields a suitable starting point for reliable estimates of the validity ranges of purely bosonic low-

energy models within the FRG. Particularly, by decomposing the flow equations of these couplings into bosonic and fermionic components, it turns out that the overall FRG scaling is almost entirely driven by the fermionic degrees of freedom (d.o.f.), even down to lowest momentum scales ($\lesssim 100$ MeV). This finding is also confirmed by functional QCD calculations [19–24] and implies a late decoupling of the composite dynamics from the fundamental fluctuations, already characterizing an upper reliability bound for the pionic description.

The intention of the present work is to extend our considerations by various points:

- (a) We verify our qualitative findings in Refs. [1–3] by applying the developed formalism to another low-energy model that is as well subject to many investigations related to the strong interaction, namely, the SO(6)-symmetric Quark-Meson-Diquark Model (QMMDM); the low-energy limit of this effective model with the corresponding low-energy couplings and the FRG scaling hierarchy of fluctuations will be (qualitatively) determined. The latter goes hand in hand with the computation of appropriate transition scales from the linear to the nonlinear symmetry realization.
- (b) Different truncation schemes within the QMDM are discussed in greater detail and the effect of higher-derivative couplings on the numerical outcome will be elucidated.
- (c) We study high-energy cutoff dependences of the low-energy couplings of the model (in an elementary setup); the couplings are thereby exclusively generated from quantum fluctuations and thus interpreted as model predictions.

In general, the QMDM serves as an effective description of two-color QCD (QC₂D), which shares many important properties with QCD itself, such as a chirally broken mesonic phase. Moreover, on the lattice, it does not

* cichutek@th.physik.uni-frankfurt.de

† fdivotgey@th.physik.uni-frankfurt.de

‡ eser@th.physik.uni-frankfurt.de

suffer from a sign problem, which makes its phase diagram much more accessible than the one of three-color QCD [25–38] (and references therein). Due to these features, QC₂D and also the QMDM have extensively been explored over the past decades, see e.g. Refs. [39–60].

This paper is organized as follows: Sec. II introduces the methods and geometric concepts of the work, where Sec. II A and Sec. II B focus on the foundations of the QMDM and the FRG, respectively. Afterwards, Sec. II C discusses the principles of the nonlinear symmetry realization of the low-energy limit of the QMDM. The results are presented in Sec. III (the generation of higher-derivative couplings is demonstrated in Sec. III A, while the transition to the nonlinear picture is carried out in Sec. III B). Finally, cutoff dependences of the low-energy couplings are studied in Sec. III C and a concluding summary as well as a scientific outlook are given in Sec. IV.

II. METHODS

A. Two-color Quantum Chromodynamics and the linear Quark-Meson-Diquark Model

Formally, QC₂D is given by an $SU(N_c = 2)$ gauge theory, which is minimally coupled to $N_f = 2$ massive Dirac-flavors of quarks (ψ) in the fundamental representation of the gauge group. Even though this appears to be a rather slight deformation of QCD, the pseudoreality of the fermion (quark) representation introduces some radical changes w.r.t. accidental symmetries of the quark sector and their respective breaking schemes. As the latter crucially affect the low-energy dynamics of QC₂D and, hence, also the construction of the QMDM, we want to briefly review these aspects in the following: QC₂D possesses an “enlarged” chiral symmetry [61, 62], i.e., $SU(4) \cong SO(6)$, which is spontaneously broken down to its $Sp(4) \cong SO(5)$ subgroup due to an antisymmetric vacuum [55, 58, 59],

$$SO(6) \longrightarrow SO(5). \quad (1)$$

This implies the occurrence of five pseudo-Nambu-Goldstone bosons (pNGBs) on the coset space $SU(4)/Sp(4) \cong SO(6)/SO(5)$; three of them are given by the pions $\vec{\pi}$ and the remaining pNGBs are identified with the real components $\pi^{4,5}$ of two diquark fields. They manifest the meson-baryon symmetry, which is furnished by the flavor symmetry of QC₂D.

Those symmetry aspects are sufficient to construct the QMDM as a simple generalization of the QMM. To this end, we make use of the local isomorphisms stated above and assign the mesonic fields to an Euclidean field space vector φ ,

$$\varphi = \begin{pmatrix} \boldsymbol{\pi} \\ \sigma \end{pmatrix}, \quad (2)$$

in which $\boldsymbol{\pi} = (\vec{\pi}, \pi^4, \pi^5)$ denotes the five-vector of pNGB

fields and σ is their chiral partner. The (Euclidean) vector φ carries the fundamental representation of $SO(6)$.

The Lagrangian of the QMDM can then be written as

$$\begin{aligned} \mathcal{L}_{\text{QMDM}} = & \frac{1}{2}(\partial_\mu \varphi) \cdot \partial^\mu \varphi - V(\rho) + h_{\text{ESB}}\sigma \\ & + \bar{\psi} \left[i\gamma^\mu \partial_\mu - y(\sigma\tau_0 + i\gamma_5 \vec{\pi} \cdot \vec{\tau}) \right] \psi \\ & + \frac{y}{2} \left[\psi^T C \gamma_5 i\sigma_2 \tau_2 (\pi^4 - i\pi^5) \psi + \text{h.c.} \right], \end{aligned} \quad (3)$$

where $\tau_0 = \mathbb{1}_2$ and $\vec{\tau}$ are the identity and the three Pauli matrices acting on flavor indices, respectively. Moreover, $C = -i\gamma_2\gamma_0$ symbolizes the charge conjugation operator and σ_2 corresponds to the second Pauli matrix in color space. The coupling y is the Yukawa interaction.

In its tree-level approximation, the scalar potential V is a quadratic polynomial in the $SO(6)$ -invariant $\rho \equiv \varphi \cdot \varphi$,

$$V(\rho) = \frac{m_0^2}{2}\rho + \frac{\lambda}{4}\rho^2, \quad (4)$$

and therefore allows for a modeling of spontaneous chiral-symmetry breaking, cf. Eq. (1). To be precise, the breaking is realized by the introduction of an order parameter σ_0 that arises in the shape of a nonvanishing vacuum expectation value for the σ field,

$$\sigma \rightarrow \sigma + \sigma_0. \quad (5)$$

In addition, the term $\sim h_{\text{ESB}}\sigma$ in Eq. (3) describes the explicit breaking of chiral symmetry by tilting the (total) potential ($V - h_{\text{ESB}}\sigma$) into the direction of the scalar resonance σ .

B. Effective action from the Functional Renormalization Group approach

Similar to Refs. [1–3], we use the FRG to determine the scale evolution of the low-energy couplings of the QMDM. In general, this method can be formulated in terms of a functional differential equation, the so-called Wetterich equation [4], that describes the FRG flow of the effective average action Γ_k ,

$$\partial_k \Gamma_k = \frac{1}{2} \text{str} \left[\left(\Gamma_k^{(2)} + R_k \right)^{-1} \partial_k R_k \right], \quad (6)$$

where k represents the FRG (energy-momentum) scale, $\Gamma_k^{(2)}$ is the two-point function, and R_k denotes an infrared (IR) regulator. The latter acts as a scale-dependent mass contribution for soft modes and implements the Wilsonian renormalization group idea of a momentum-shell-wise integration over the quantum fluctuations of the system [63–65]. Hence, the effective average action Γ_k is a functional that interpolates between the classical action, initialized at an ultraviolet (UV) cutoff Λ_{UV} , and the full effective (quantum) action $\Gamma_{k=0} \equiv \Gamma$ in the IR.

The structure of Eq. (6) implies an infinite tower of coupled differential equations. Thus our ability to solve

the Wetterich equation depends on an appropriate truncation of correlation functions. In this light, we choose the following derivative expansion for the Euclidean effective average action:

$$\begin{aligned} \Gamma_k = \int_x \left\{ \frac{Z_k}{2} (\partial_\mu \varphi) \cdot \partial_\mu \varphi + U_k(\rho) - h_{\text{ESB}} \sigma \right. \\ + C_{2,k} (\varphi \cdot \partial_\mu \varphi)^2 + Z_{2,k} \varphi^2 (\partial_\mu \varphi) \cdot \partial_\mu \varphi \\ - C_{3,k} [(\partial_\mu \varphi) \cdot \partial_\mu \varphi]^2 - C_{4,k} [(\partial_\mu \varphi) \cdot \partial_\nu \varphi]^2 \\ - C_{5,k} \varphi \cdot (\partial_\mu \partial_\mu \varphi) (\partial_\nu \varphi) \cdot \partial_\nu \varphi \\ - C_{6,k} \varphi^2 (\partial_\mu \partial_\nu \varphi) \cdot \partial_\mu \partial_\nu \varphi \\ - C_{7,k} (\varphi \cdot \partial_\mu \partial_\nu \varphi)^2 - C_{8,k} \varphi^2 (\partial_\mu \partial_\mu \varphi)^2 \\ + \bar{\psi} \left[Z_k^\psi \gamma_\mu \partial_\mu + y_k (\sigma \tau_0 + i \gamma_5 \vec{\pi} \cdot \vec{\tau}) \right] \psi \\ \left. + \frac{y_k}{2} \left[\psi^T C \gamma_5 i \sigma_2 \tau_2 (\pi^4 - i \pi^5) \psi + \text{h.c.} \right] \right\}. \quad (7) \end{aligned}$$

Here, we replaced Eq. (4) by the effective potential $U_k(\rho)$ and established an obvious short-hand notation for the space-time integration. Furthermore, besides a scale-dependent Yukawa coupling y_k , we also introduced wave-function renormalization factors for both the bosonic and fermionic d.o.f., Z_k and Z_k^ψ , respectively. Finally, as we are interested in the low-energy couplings of the QMDM, we supplemented the bosonic sector of Eq. (3) by complete sets of higher-derivative couplings of $\mathcal{O}(\varphi^4, \partial^2)$ and $\mathcal{O}(\varphi^4, \partial^4)$. The truncation (7) goes substantially beyond the commonly employed local potential approximation (LPA) (only the scale dependence of the effective potential U_k is considered) or its minimal extension known as the LPA' (involving wave-function renormalization). The chosen set of higher-derivative couplings conforms with the recently published fourth-order derivative expansion in the (generic) $\text{SO}(N)$ -model [11, 66] [and Eq. (7) even also includes fermionic d.o.f.].

As an immediate consequence of spontaneous chiral-symmetry breaking, the $\text{SO}(6)$ -symmetric wave-function renormalization Z_k splits into two separate contributions associated with the π fields and the σ ,

$$Z_k^\pi = Z_k + 2\sigma^2 Z_{2,k} - 2\sigma^2 p^2 (C_{6,k} + C_{8,k}), \quad (8)$$

$$\begin{aligned} Z_k^\sigma = Z_k + 2\sigma^2 (C_{2,k} + Z_{2,k}) \\ - 2\sigma^2 p^2 (C_{6,k} + C_{7,k} + C_{8,k}), \quad (9) \end{aligned}$$

where p refers to the external momentum from the functional derivatives w.r.t. the bosonic fields; cf. the Appendix. Using the above expressions and the fermionic wave-function renormalization factor, we define the renormalized (physical) fields and model parameters as

$$\begin{aligned} \tilde{\pi} = \sqrt{Z_k^\pi} \pi, \quad \tilde{\sigma} = \sqrt{Z_k^\sigma} \sigma, \quad \tilde{\psi} = \sqrt{Z_k^\psi} \psi, \\ \tilde{h}_{\text{ESB}} = \frac{h_{\text{ESB}}}{\sqrt{Z_k^\pi}}, \quad \tilde{y}_k = \frac{y_k}{\sqrt{Z_k^\pi} Z_k^\psi}, \quad (10) \\ \tilde{C}_{i,k} = \frac{C_{i,k}}{(Z_k^\pi)^2}, \quad i = 1, \dots, 8, \quad \tilde{Z}_{2,k} = \frac{Z_{2,k}}{(Z_k^\pi)^2}. \end{aligned}$$

The renormalized quantities will lead to a well-normalized kinetic term of the effective action in the upcoming Section. For the sake of simplicity, Eqs. (8) and (9) are evaluated at $p = 0$ during the flow. The coupling $C_{1,k}$ in Eq. (10) corresponds to the momentum-independent quartic interaction in the effective potential U_k , see also the Appendix.

C. Nonlinear effective pseudo-Nambu-Goldstone action

The low-energy limit of the $\text{SO}(6)$ -invariant QMDM is a nonlinear effective model over the vacuum manifold $\text{SU}(4)/\text{Sp}(4) \cong \text{SO}(6)/\text{SO}(5)$. It is generated by eliminating the ‘‘heavy’’ dynamics of all non-pNGB fields from the renormalized effective average action. To this end, along the lines of Ref. [2], we start with the fermionic sector of the QMDM and drop all operators depending on the quark fields ψ , as their respective contributions to the low-energy couplings are already captured by the FRG integration and only tree-level amplitudes are necessary to cover quantum effects (based on Γ). Afterwards, we are left with a purely bosonic model that has the same structure as the usual $\text{SO}(6)$ Linear Sigma Model.

Now, in order to eliminate the massive isoscalar component σ of the vector φ in Eq. (2), we make use of the diffeomorphism between the vacuum manifold and the five-sphere, $\text{SO}(6)/\text{SO}(5) \cong S^5$, and rotate the renormalized bosonic field configuration into a frame that yields a clear separation between its light and massive modes,

$$\begin{aligned} \tilde{\varphi} &\equiv \sqrt{Z_k^\pi} \varphi = \Sigma(\tilde{\zeta}) \tilde{\phi}, \\ \tilde{\phi} &= (\mathbf{0}, \tilde{\theta}). \quad (11) \end{aligned}$$

The field $\tilde{\theta} = \sqrt{\tilde{\varphi} \cdot \tilde{\varphi}}$ describes the radial excitation of Eq. (2). In contrast, the pNGB d.o.f. constitute a set of coordinates on S^5 and are written as $\tilde{\zeta}^a$, $a = 1, \dots, 5$. From the technical viewpoint, the transformation $\Sigma(\tilde{\zeta})$ associates each point on $\text{SO}(6)/\text{SO}(5)$, i.e., each (left) coset, with an element of $\text{SO}(6)$ and is thus interpreted as a coset representative. Choosing stereographic projections as coordinates,

$$\tilde{\zeta}^a = \frac{\tilde{\pi}^a}{\tilde{\theta} + \tilde{\sigma}}, \quad a = 1, \dots, 5, \quad (12)$$

its explicit form is given by

$$\Sigma(\tilde{\zeta}) = \begin{pmatrix} \delta^a_b - \frac{2\tilde{\zeta}^a \tilde{\zeta}_b}{1+\tilde{\zeta}^2} & \frac{2\tilde{\zeta}^a}{1+\tilde{\zeta}^2} \\ -\frac{2\tilde{\zeta}_b}{1+\tilde{\zeta}^2} & \frac{1-\tilde{\zeta}^2}{1+\tilde{\zeta}^2} \end{pmatrix}. \quad (13)$$

Apart from its geometric meaning, the coset representative can also be used to define further objects, such as the Maurer-Cartan form α_μ ,

$$\alpha_\mu(\tilde{\zeta}) = \Sigma(\tilde{\zeta})^{-1} \partial_\mu \Sigma(\tilde{\zeta}). \quad (14)$$

It takes its values in the Lie algebra $\mathfrak{so}(6)$ and therefore admits an expansion of the form

$$\alpha_\mu(\tilde{\zeta}) = ie_\alpha^a(\tilde{\zeta})\partial_\mu\tilde{\zeta}^\alpha x_a + i\omega_\alpha^i(\tilde{\zeta})\partial_\mu\tilde{\zeta}^\alpha s_i, \quad (15)$$

where $\alpha = 1, \dots, 5$ represents a ‘‘curved’’ coset index and $x_a, a = 1, \dots, 5$, as well as $s_i, i = 1, \dots, 10$, denote the broken and unbroken generators of $\text{SO}(6)$, respectively. The 15 generators J_b^a (skew-symmetric matrices) in the fundamental representation fulfill the relation

$$(J_b^a)^m_n = -i(\delta^{am}\delta_{bn} - \delta^a_n\delta^m_b), \quad (16)$$

with the indices $a, b, m, n = 1, \dots, 6, a < b$, and $x_a = J_a^6$. These considerations are generalizations of the generators and transformation properties of the geometric objects quoted in Ref. [2].

In the following, we will mainly be interested in the coefficients proportional to the broken generators [the coefficients $\omega_\alpha^i(\tilde{\zeta})$ are not of further interest here], i.e.,

$$e_\alpha^a(\tilde{\zeta}) = \frac{2\delta_\alpha^a}{1 + \tilde{\zeta}^2}. \quad (17)$$

This identity derives from Eqs. (13) and (15). The coefficients $e_\alpha^a(\tilde{\zeta})$ define a vielbein on $\text{SO}(6)/\text{SO}(5)$ and give rise to the metric

$$g_{\alpha\beta}(\tilde{\zeta}) \equiv \delta_{ab}e_\alpha^a(\tilde{\zeta})e_\beta^b(\tilde{\zeta}) = \frac{4\delta_{\alpha\beta}}{(1 + \tilde{\zeta}^2)^2}. \quad (18)$$

Finally, inserting Eq. (11) into the remaining Linear Sigma Model and restricting the bosonic dynamics to the vacuum manifold, i.e., setting the radial excitation to the pion decay constant f_π ,

$$\tilde{\theta} = f_\pi, \quad (19)$$

the renormalized effective pNGB action takes the following form:

$$\begin{aligned} \Gamma_k = \int_x \left[\frac{f_\pi^2}{2} g_{\alpha\beta}(\nabla_\mu\tilde{\zeta}^\alpha)\nabla_\mu\tilde{\zeta}^\beta \right. \\ - (\tilde{C}_{6,k} + \tilde{C}_{8,k})f_\pi^4 g_{\alpha\beta}(\nabla_\mu\nabla_\mu\tilde{\zeta}^\alpha)\nabla_\nu\nabla_\nu\tilde{\zeta}^\beta \\ - (\tilde{C}_{3,k} - \tilde{C}_{5,k} + \tilde{C}_{6,k} + \tilde{C}_{7,k} + \tilde{C}_{8,k})f_\pi^4 \\ \quad \times g_{\alpha\beta}g_{\gamma\delta}(\nabla_\mu\tilde{\zeta}^\alpha)(\nabla_\mu\tilde{\zeta}^\beta)(\nabla_\nu\tilde{\zeta}^\gamma)\nabla_\nu\tilde{\zeta}^\delta \\ - \tilde{C}_{4,k}f_\pi^4 g_{\alpha\beta}g_{\gamma\delta}(\nabla_\mu\tilde{\zeta}^\alpha)(\nabla_\nu\tilde{\zeta}^\beta)(\nabla_\mu\tilde{\zeta}^\gamma)\nabla_\nu\tilde{\zeta}^\delta \\ \left. - \tilde{h}_{\text{ESB}}f_\pi \frac{1 - \tilde{\zeta}^2}{1 + \tilde{\zeta}^2} \right], \quad (20) \end{aligned}$$

where the action of the covariant derivative ∇_μ onto the pNGB fields as well as their space-time derivatives is defined in the usual way, see Ref. [2]. The above equation resembles the most general ansatz for the derivative expansion of the $\text{SO}(6)$ Nonlinear Sigma Model up to (and including) $\mathcal{O}(\partial^4)$ [67, 68]. However, as a consequence of explicit chiral-symmetry breaking, Eq. (20) also features a potential for the pNGB fields.

Similar to Ref. [2], the low-energy limit of the QMDM is obtained by expanding Eq. (20) up to fourth order in the rescaled pNGB fields $\tilde{\Pi}^a = 2f_\pi\zeta^a$, $a = 1, \dots, 5$; one arrives at

$$\begin{aligned} \Gamma_k = \int_x \left\{ \frac{1}{2}(\partial_\mu\tilde{\Pi}_a)\partial_\mu\tilde{\Pi}^a + \frac{1}{2}\tilde{\mathcal{M}}_{\Pi,k}^2\tilde{\Pi}_a\tilde{\Pi}^a \right. \\ - \tilde{C}_{1,k}(\tilde{\Pi}_a\tilde{\Pi}^a)^2 + \tilde{Z}_{2,k}\tilde{\Pi}_a\tilde{\Pi}^a(\partial_\mu\tilde{\Pi}_b)\partial_\mu\tilde{\Pi}^b \\ - \tilde{C}_{3,k}\left[(\partial_\mu\tilde{\Pi}_a)\partial_\mu\tilde{\Pi}^a\right]^2 \\ - \tilde{C}_{4,k}\left[(\partial_\mu\tilde{\Pi}_a)\partial_\nu\tilde{\Pi}^a\right]^2 \\ - \tilde{C}_{5,k}\tilde{\Pi}_a(\partial_\mu\partial_\mu\tilde{\Pi}^a)(\partial_\nu\tilde{\Pi}_b)\partial_\nu\tilde{\Pi}^b \\ - \tilde{C}_{6,k}\tilde{\Pi}_a\tilde{\Pi}^a(\partial_\mu\partial_\nu\tilde{\Pi}_b)\partial_\mu\partial_\nu\tilde{\Pi}^b \\ \left. - \tilde{C}_{8,k}\tilde{\Pi}_a\tilde{\Pi}^a(\partial_\mu\partial_\mu\tilde{\Pi}_b)\partial_\nu\partial_\nu\tilde{\Pi}^b\right\}, \quad (21) \end{aligned}$$

where we defined the (squared) pNGB mass as

$$\tilde{\mathcal{M}}_{\Pi,k}^2 = \frac{\tilde{h}_{\text{ESB}}}{f_\pi}. \quad (22)$$

The low-energy couplings of the QMDM in Eq. (21) are functions of the linear model parameters and the pion decay constant f_π ,

$$\begin{aligned} \tilde{C}_{1,k} &= \frac{\tilde{\mathcal{M}}_{\Pi,k}^2}{8f_\pi^2}, \\ \tilde{Z}_{2,k} &= -\frac{1}{4f_\pi^2}, \\ \tilde{C}_{3,k} &= \tilde{C}_{3,k} - \tilde{C}_{5,k} + \tilde{C}_{7,k} + 2(\tilde{C}_{6,k} + \tilde{C}_{8,k}), \\ \tilde{C}_{4,k} &= \tilde{C}_{4,k}, \\ \tilde{C}_{5,k} &= 2(\tilde{C}_{6,k} + \tilde{C}_{8,k}), \\ \tilde{C}_{6,k} &= -\tilde{C}_{6,k} - \tilde{C}_{8,k}, \\ \tilde{C}_{8,k} &= \frac{1}{2}(\tilde{C}_{6,k} + \tilde{C}_{8,k}). \end{aligned} \quad (23)$$

We observe that the geometric constraint of fixing the dynamics of the linear model to the five-sphere eliminates the couplings $\tilde{C}_{2,k}$ and $\tilde{C}_{7,k}$. Additionally, the couplings $\tilde{C}_{5,k}$, $\tilde{C}_{6,k}$, and $\tilde{C}_{8,k}$ exhibit a linear dependence w.r.t. the sum $\tilde{C}_{6,k} + \tilde{C}_{8,k}$.

III. RESULTS

In the present qualitative study, we shed light on the FRG scaling behavior of higher-derivative couplings of the $\text{SO}(6)$ -invariant QMDM. The UV values of the scale-dependent variables in Eq. (7) are tuned such that physical values for the meson and (constituent) quark masses are produced in the IR limit, if possible [following ‘‘usual’’ QCD [69]]: $M_\pi \simeq 139$ MeV, $M_\sigma \simeq 400 - 500$ MeV, and $M_\psi \simeq 300 - 330$ MeV (about one third of the proton

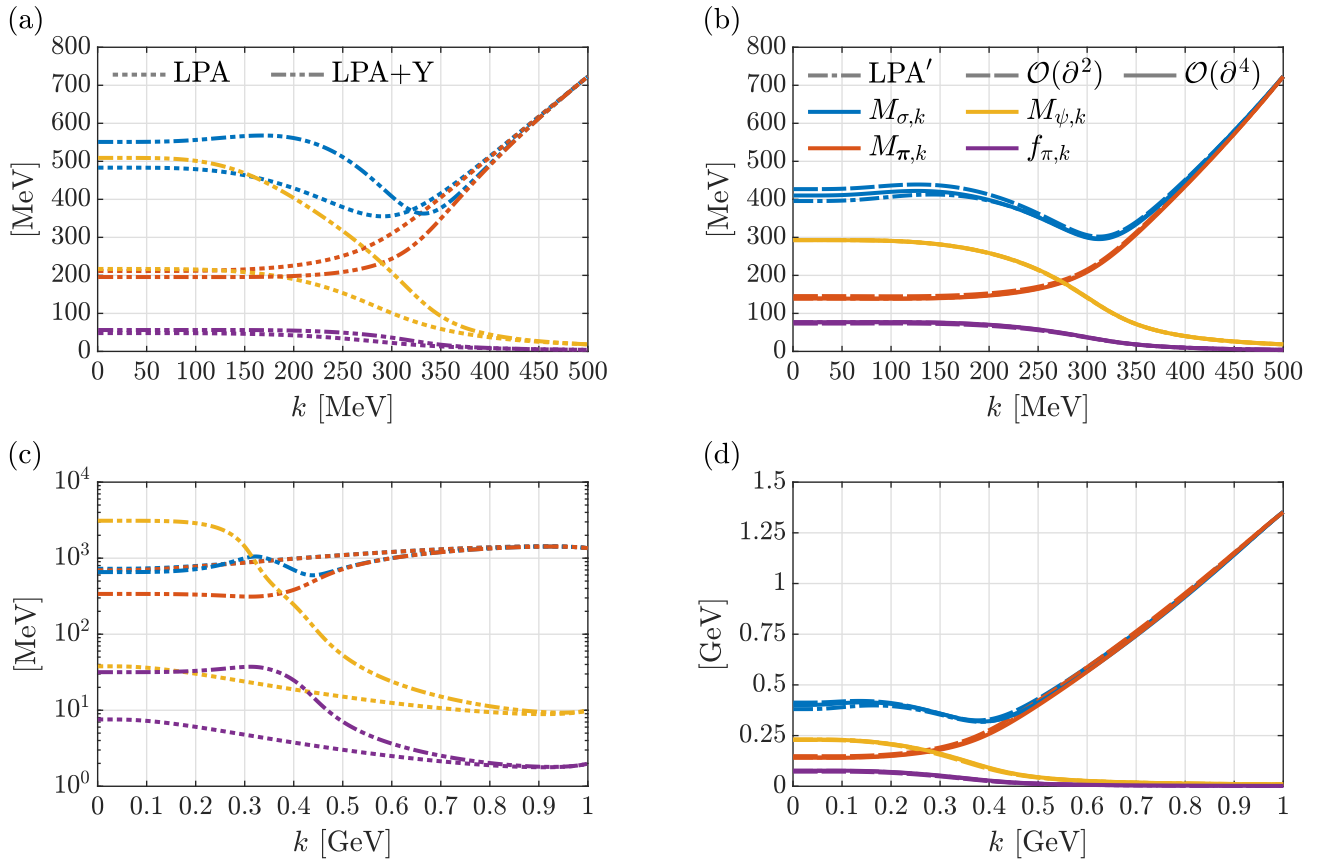


Figure 1. Scale-dependent renormalized masses and the pion decay constant in various truncations of the SO(6) QMDM. Two different UV-cutoff scenarios are shown: $\Lambda_{\text{UV}} = 500$ MeV [subfigures (a) and (b)] and $\Lambda_{\text{UV}} = 1$ GeV [subfigures (c) and (d)]; the legends of subfigures (a) and (b) apply to all panels.

Table I. IR parameters. All parameters are evaluated at $k = k_{\text{IR}} = 0.5$ MeV.

Parameter	$\Lambda_{\text{UV}} = 500$ MeV					$\Lambda_{\text{UV}} = 1$ GeV				
	$\mathcal{O}(\partial^4)$	$\mathcal{O}(\partial^2)$	LPA'	LPA+Y	LPA	$\mathcal{O}(\partial^4)$	$\mathcal{O}(\partial^2)$	LPA'	LPA+Y	LPA
M_π [MeV]	139.0	145.5	139.1	195.7	211.5	140.8	148.6	141.9	338.8	693.0
M_σ [MeV]	410.1	426.9	395.6	551.0	483.3	400.9	412.7	380.5	656.2	725.5
M_ψ [MeV]	292.6	293.0	292.9	509.0	216.9	230.4	228.5	230.7	3106.9	37.8
f_π [MeV]	76.9	73.3	76.8	56.3	48.2	76.9	72.2	76.2	31.7	7.6
\tilde{y}	3.81	4.00	3.81	9.04	4.50	2.99	3.16	3.03	98.08	5.00
Z^π	2.10	1.93	2.10	1.00	1.00	5.68	5.19	5.62	1.00	1.00
Z^σ	1.78	1.62	1.92	1.00	1.00	5.70	5.19	6.29	1.00	1.00
Z^ψ	1.17	1.18	1.17	1.00	1.00	1.24	1.24	1.24	1.00	1.00
$\tilde{\alpha}_1/(10f_\pi^2)$	0.16	0.20	0.16	0.38	1.39	0.17	0.24	0.18	6.04	7.39×10^2
\tilde{C}_1	-2.61	-3.07	-2.61	-9.46	-9.92	-2.99	-3.61	-3.08	-40.93	-90.65
$\tilde{\alpha}_3 f_\pi^2$	-0.56	-0.61	-0.58	26.09	-3.58	2.78	2.80	2.72	80.85	0.17
$\tilde{\alpha}_4 f_\pi^4/10$	-1.04	-1.19	-1.03	-16.22	-0.83	-1.11	-1.00	-1.07	6.05	0.01
$\tilde{\alpha}_5 f_\pi^6/10^2$	0.79	0.86	0.78	4.11	0.41	0.69	0.55	0.65	-2.16	-8.58×10^{-5}
$\tilde{\alpha}_6 f_\pi^8/10^3$	-0.73	-0.75	-0.71	4.81	-0.22	-0.60	-0.41	-0.55	-1.11	1.50×10^{-6}

mass). However, the desired value for the pion decay constant, $f_\pi \simeq 76$ MeV, which is related to the scale-

dependent minimum of the effective potential U_k , is $\sqrt{N_c}$ -scaled as compared to QCD ($f_\pi \simeq 93$ MeV). The IR

values of the higher-derivative interactions, which are initialized at zero in the UV, are understood as model predictions.

Besides the explicit investigation of different truncations of the QMDM [LPA, LPA+Y (LPA and the flow of the Yukawa coupling y_k), LPA', couplings at $\mathcal{O}(\partial^2)$, and couplings at $\mathcal{O}(\partial^4)$], we choose two different UV-cutoff scenarios, namely, $\Lambda_{\text{UV}} = 500$ MeV and $\Lambda_{\text{UV}} = 1$ GeV. These two scenarios give insights into possible tuning procedures and provide a first (rather simple and qualitative) estimate of UV-cutoff dependences of the higher-derivative interactions and, hence, the low-energy couplings of the QMDM. Both chosen scales are frequently used in FRG studies of the model [55, 59].

The FRG flow is stopped at $k \equiv k_{\text{IR}} = 0.5$ MeV to reduce numerical costs; at $k = k_{\text{IR}}$, there is no longer any scale dependence. Further details about the FRG flow equations and their numerical solutions are deferred to the Appendix.

A. Linear model: Flow of the higher-derivative couplings

The scale-dependent squared meson and quark masses are derived from the effective potential and the Yukawa interaction as

$$m_{\pi,k}^2 = 2U'_k, \quad m_{\sigma,k}^2 = 2U'_k + 4\rho U''_k, \quad m_{\psi,k}^2 = y_k^2 \rho. \quad (24)$$

These expressions are evaluated at the scale-dependent minimum $\rho_{0,k}$ of the term $U_k - h_{\text{ESB}}\sqrt{\rho}$. The corresponding renormalized masses are given by

$$M_{\pi,k}^2 = \frac{m_{\pi,k}^2}{Z_{\pi}^k}, \quad M_{\sigma,k}^2 = \frac{m_{\sigma,k}^2}{Z_{\sigma}^k}, \quad M_{\psi,k}^2 = \frac{m_{\psi,k}^2}{(Z_{\psi}^k)^2}. \quad (25)$$

For the two different scenarios, we were able to find the following values for the (renormalized) masses and the pion decay constants:

- $M_{\pi,k_{\text{IR}}} = 139.0$ MeV, $M_{\sigma,k_{\text{IR}}} = 410.1$ MeV, and $M_{\psi,k_{\text{IR}}} = 292.6$ MeV, as well as $f_{\pi} = 76.9$ MeV ($\Lambda_{\text{UV}} = 500$ MeV);
- $M_{\pi,k_{\text{IR}}} = 140.8$ MeV, $M_{\sigma,k_{\text{IR}}} = 400.9$ MeV, and $M_{\psi,k_{\text{IR}}} = 230.4$ MeV, as well as $f_{\pi} = 76.9$ MeV ($\Lambda_{\text{UV}} = 1$ GeV).

These findings are collected in Table I in the column “ $\mathcal{O}(\partial^4)$ ” (for both chosen UV cutoffs), which stands for the “full” flow, i.e., we take into account all higher-derivative couplings introduced in Eq. (7). We remark that the generated masses and decay constants are in the “physical” ranges mentioned above, except for the quark masses, which appear to be slightly too light. The fact that it was harder to find reasonable values for the larger cutoff of 1 GeV already points out limitations of the model and (possibly) exceeded validity ranges.

Concerning the different truncation schemes, we plot in Fig. 1 the entire evolution of the scale-dependent masses and the pion decay constant for all approximations (the starting values in the UV are kept constant). It reveals that the largest corrections (deviations) come from the inclusion (neglect) of the FRG flow of the wave-function renormalization, cf. Fig. 1(a) in comparison to Fig. 1(b). Also, the flow of the Yukawa coupling y_k has a relatively large influence on the outcome in the IR, which confirms the study in Ref. [59]; thus the inclusion of wave-function renormalizations is of major importance for a consistent truncation scheme at this specific momentum-independent level.

These observations are even more drastic in the cutoff scenario of 1 GeV, where in the “lower” truncations LPA and LPA+Y the results are partly of a different order of magnitude, cf. Fig. 1(c) and Fig. 1(d). In particular, chiral symmetry cannot even be considered as (substantially) broken in the LPA truncation; the quantities $M_{\pi,k_{\text{IR}}}$ and $M_{\sigma,k_{\text{IR}}}$ only differ by less than 40 MeV and the decay constant stays below 10 MeV, see the last column in Table I. In the “higher” truncations [LPA', $\mathcal{O}(\partial^2)$, and $\mathcal{O}(\partial^4)$], the energy-momentum scale of chiral-symmetry breaking is shifted from around 300–400 MeV to larger values of 400–500 MeV [Fig. 1(b) and Fig. 1(d)], when increasing the UV cutoff from 500 MeV to 1 GeV. The breaking is signaled by the growing mass split between the pNGB fields and the σ occurring in this region. One further finds that the observables within the LPA' truncation are in some instances good approximations to the final results of $\mathcal{O}(\partial^4)$, e.g. for the pion mass listed in the first row of Table I or the pion decay constant in the fourth row. This is consistent with Ref. [1] and could be explained by cancellation effects in the wave-function renormalization factors (8) and (9) beyond the LPA'.

The explicit FRG flows of the wave-function renormalization factors and the Yukawa coupling are found in the Appendix. Moreover, Table I contains their IR-limit values as well as the renormalized Taylor coefficients $\tilde{\alpha}_{n,k}$, $n = 1, \dots, 6$, which were used to numerically solve the flow equation for the effective potential U_k ; see once more the Appendix for details. The coupling $\tilde{\alpha}_{2,k}$ is replaced by its identification (A.16) with the (momentum-independent) quartic interaction. At this point, we register that these coefficients reflect again the large differences in the effective potential w.r.t. the various investigated truncations.

Figure 2 demonstrates how the higher-derivative couplings are (exclusively) generated from quantum fluctuations, starting from zero at $\Lambda_{\text{UV}} = 500$ MeV [Fig. 2(a) and Fig. 2(b)] and $\Lambda_{\text{UV}} = 1$ GeV [Fig. 2(c) and Fig. 2(d)]. Here, we decided to present the $\mathcal{O}(\partial^4)$ -couplings first as they are more relevant for the low-energy limit in the nonlinear realization, cf. Eq. (23); the $\mathcal{O}(\partial^2)$ -couplings do not enter the limit explicitly. Comparing the upper to the lower panels, we notice that the evolution of the renormalized higher-derivative couplings becomes “flatter” in the high-energy regime for the scenario with a

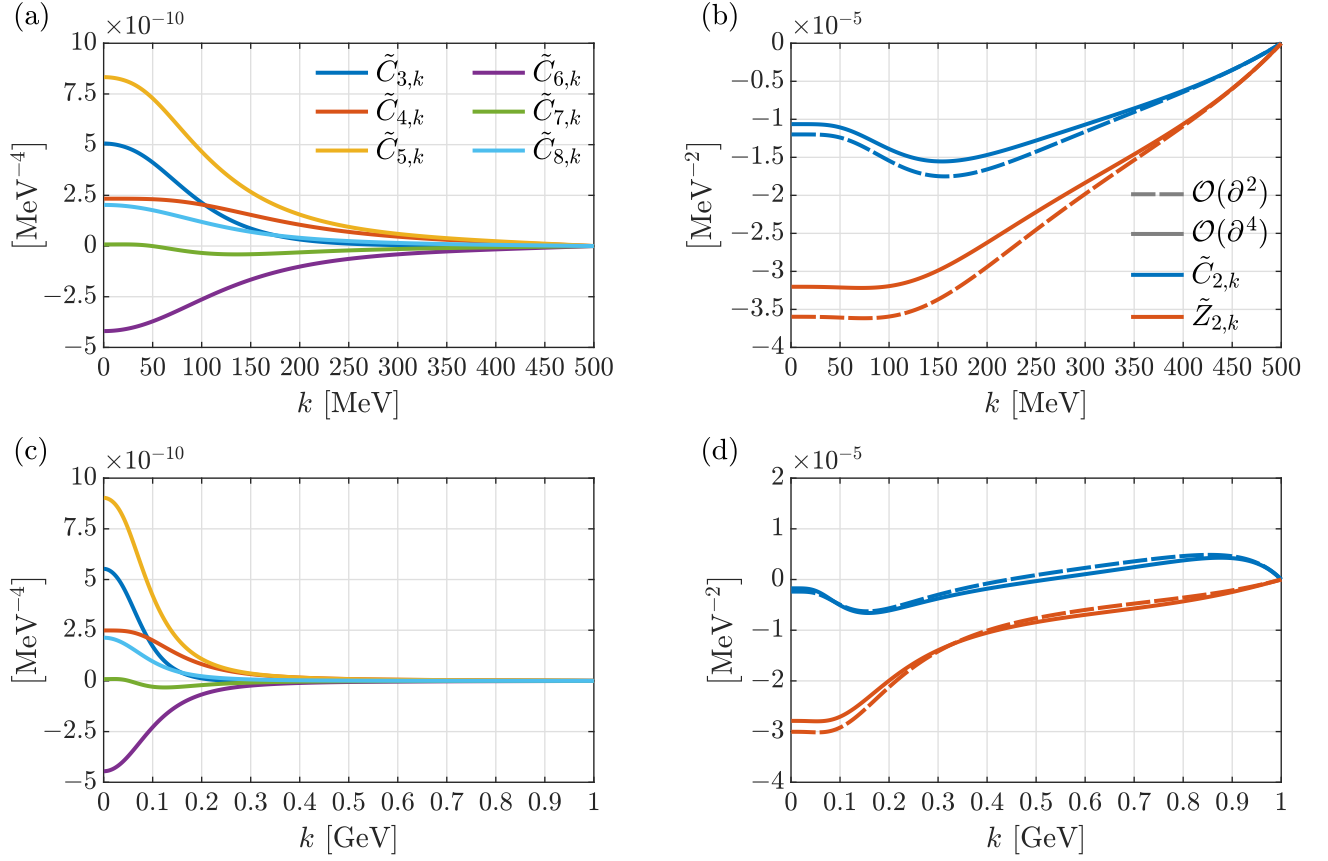


Figure 2. Flow of higher-derivative couplings of the SO(6) QMDM (linear symmetry realization). The legends in subfigures (a) and (b) apply to all panels.

Table II. Higher-derivative couplings (linear model), meson and quark masses, and pion decay constants. The scale of initialization of the higher-derivative interactions, Λ_C , is given below the (general) cutoff scale Λ_{UV} , $\Lambda_C = \text{factor} \times \Lambda_{UV}$. All couplings, masses, and decay constants are evaluated at $k = k_{IR} = 0.5$ MeV.

Parameter	$\Lambda_{UV} = 500$ MeV					$\Lambda_{UV} = 1$ GeV										
	1.0	0.8	0.6	0.4	0.2	1.0	0.9	0.8	0.7	0.6	0.5	0.4	0.3	0.2	0.1	
M_π [MeV]	139.0	139.2	139.2	139.1	139.1	140.8	140.9	141.1	141.3	141.5	141.7	141.8	142.0	142.0	141.9	
M_σ [MeV]	410.1	409.8	407.4	401.3	395.9	400.9	400.6	400.5	400.2	399.7	398.8	396.9	393.2	386.4	380.8	
M_ψ [MeV]	292.6	292.8	292.8	292.9	292.9	230.4	230.5	230.6	230.6	230.6	230.6	230.6	230.7	230.7	230.7	
f_π [MeV]	76.9	76.8	76.7	76.8	76.8	76.9	76.9	76.7	76.6	76.5	76.3	76.2	76.1	76.1	76.2	
$\tilde{C}_2 [1/f_\pi^2] \times 10$	-0.63	-0.48	-0.18	0.26	0.24	-0.10	-0.11	-0.11	-0.11	-0.10	-0.08	-0.02	0.11	0.33	0.23	
$\tilde{Z}_2 [1/f_\pi^2] \times 10$	-1.89	-1.68	-1.26	-0.56	-0.01	-1.65	-1.65	-1.64	-1.63	-1.60	-1.56	-1.45	-1.22	-0.71	-0.06	
$\tilde{C}_3 [1/f_\pi^4] \times 10^2$	1.77	1.80	1.86	1.87	1.15	1.94	1.93	1.93	1.92	1.92	1.92	1.94	1.98	2.04	1.43	
$\tilde{C}_4 [1/f_\pi^4] \times 10^2$	0.82	0.78	0.68	0.44	0.08	0.87	0.87	0.87	0.86	0.85	0.84	0.82	0.76	0.58	0.15	
$\tilde{C}_5 [1/f_\pi^4] \times 10^2$	2.91	2.90	2.86	2.62	1.42	3.16	3.15	3.14	3.12	3.11	3.10	3.09	3.09	2.96	1.79	
$\tilde{C}_6 [1/f_\pi^4] \times 10^2$	-1.47	-1.44	-1.38	-1.17	-0.55	-1.56	-1.56	-1.55	-1.55	-1.54	-1.54	-1.53	-1.49	-1.35	-0.75	
$\tilde{C}_7 [1/f_\pi^4] \times 10^2$	0.03	0.04	0.07	0.16	0.18	0.03	0.03	0.02	0.02	0.02	0.02	0.02	0.04	0.12	0.16	
$\tilde{C}_8 [1/f_\pi^4] \times 10^2$	0.71	0.70	0.69	0.61	0.30	0.75	0.75	0.74	0.74	0.74	0.74	0.74	0.73	0.69	0.41	

larger UV cutoff. Such a behavior was already anticipated in the study of the SO(4)-symmetric QMM [2] and it underlines their character as couplings parametrizing

low-energy operators, e.g. the couplings $\tilde{C}_{i,k}$, $i = 3, \dots, 8$, in Fig. 2(c) become solely relevant below $k \simeq 500$ MeV. The relatively steep slope of the curves close to Λ_{UV} in

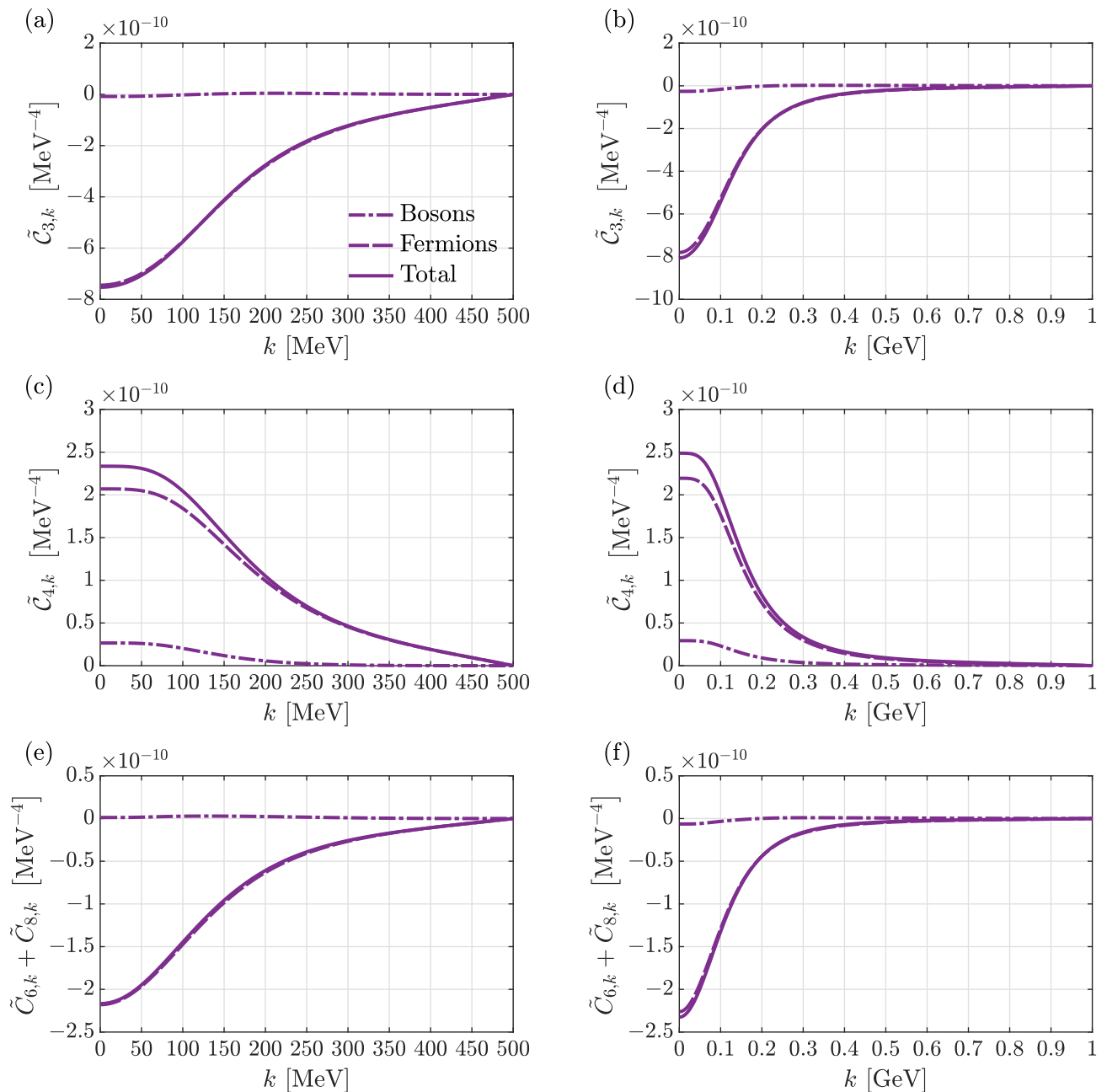


Figure 3. FRG scale evolution of the low-energy couplings of the SO(6)-symmetric QMDM. The total flows (solid lines) are divided into contributions from bosonic and fermionic quantum fluctuations (dash-dotted and dashed lines, respectively). The legend in subfigure (a) is valid for all panels. Since the couplings $\tilde{C}_{5,k}$, $\tilde{C}_{6,k}$, and $\tilde{C}_{8,k}$ are linearly dependent according to Eq. (23), we only show the sum $\tilde{C}_{6,k} + \tilde{C}_{8,k}$ in subfigures (e) and (f).

Fig. 2(b) and Fig. 2(d) indicates, however, that the couplings $\tilde{C}_{2,k}$ and $\tilde{Z}_{2,k}$ should still be present in the UV. Finally, the effect of the FRG flow of the couplings of $\mathcal{O}(\partial^4)$ onto these $\mathcal{O}(\partial^2)$ -couplings shrinks from Fig. 2(b) to Fig. 2(d) (see the dashed and solid lines). The precise IR values of the higher-derivative couplings are discussed in Sec. III C, together with a qualitative estimate of their cutoff dependences.

B. Nonlinear model: Transition to the low-energy couplings

A physically meaningful transition scale to the nonlinear model is reached upon a decoupling of all heavy d.o.f. (i.e., heavier than the pNGBs) from the FRG flow. Nevertheless, Eq. (23) allows us to map the linear model with its higher-derivative interactions on all energy-momentum scales onto the nonlinear counterpart,

Table III. Low-energy couplings (nonlinear model). The scale of initialization of the higher-derivative interactions, Λ_C , is given below the (general) cutoff scale Λ_{UV} , $\Lambda_C = \text{factor} \times \Lambda_{UV}$. All couplings are evaluated at $k = k_{IR} = 0.5$ MeV. The renormalized pion mass $\mathcal{M}_{\Pi,k}$ is given in Table II, $\mathcal{M}_{\Pi,k} \equiv M_{\pi,k}$.

Coupling	$\Lambda_{UV} = 500$ MeV					$\Lambda_{UV} = 1$ GeV									
	1.0	0.8	0.6	0.4	0.2	1.0	0.9	0.8	0.7	0.6	0.5	0.4	0.3	0.2	0.1
$\tilde{\mathcal{C}}_1 \times 10$	4.09	4.10	4.11	4.10	4.09	4.18	4.20	4.22	4.25	4.28	4.31	4.33	4.35	4.35	4.34
$\tilde{\mathcal{Z}}_2 [1/f_\pi^2] \times 10$	-2.50	-2.50	-2.50	-2.50	-2.50	-2.50	-2.50	-2.50	-2.50	-2.50	-2.50	-2.50	-2.50	-2.50	-2.50
$\tilde{\mathcal{C}}_3 [1/f_\pi^4] \times 10^2$	-2.63	-2.55	-2.32	-1.71	-0.59	-2.83	-2.82	-2.81	-2.80	-2.78	-2.76	-2.71	-2.58	-2.13	-0.88
$\tilde{\mathcal{C}}_4 [1/f_\pi^4] \times 10^2$	0.82	0.78	0.68	0.44	0.08	0.87	0.87	0.87	0.86	0.85	0.84	0.82	0.76	0.58	0.15
$\tilde{\mathcal{C}}_5 [1/f_\pi^4] \times 10^2$	-1.51	-1.48	-1.39	-1.12	-0.49	-1.63	-1.63	-1.62	-1.61	-1.60	-1.59	-1.58	-1.52	-1.33	-0.69
$\tilde{\mathcal{C}}_6 [1/f_\pi^4] \times 10^2$	0.76	0.74	0.69	0.56	0.25	0.82	0.81	0.81	0.81	0.80	0.80	0.79	0.76	0.67	0.34
$\tilde{\mathcal{C}}_8 [1/f_\pi^4] \times 10^2$	-0.38	-0.37	-0.35	-0.28	-0.12	-0.41	-0.41	-0.41	-0.40	-0.40	-0.40	-0.39	-0.38	-0.33	-0.17

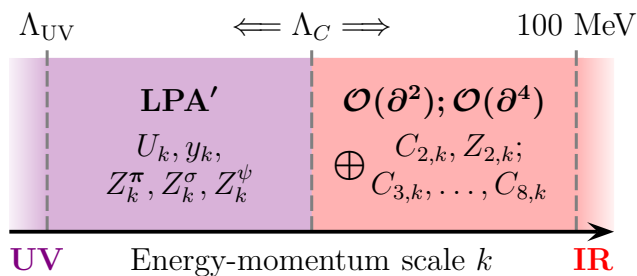


Figure 4. Study of cutoff dependences. The cutoff Λ_C for the higher-derivative couplings $C_{2,k}$, $Z_{2,k}$, and $C_{i,k}$, $i = 3, \dots, 8$, varies between 100 MeV and the overall UV cutoff Λ_{UV} (in steps of 100 MeV each). These enter the dynamics at Λ_C in addition to (\oplus) the LPA' truncation (i.e., the flow of the effective potential U_k , the Yukawa coupling y_k , as well as the wave-function renormalization factors Z_k^π , Z_k^σ , and Z_k^ψ); the LPA' flow is initialized at Λ_{UV} .

which grants full access to the entire scaling behavior of the low-energy couplings.

Figure 3 illustrates the mapping onto the nonlinear pNGB action (21), carried out on all scales k within the respective UV-cutoff scenario. The flow of the low-energy couplings $\tilde{\mathcal{C}}_{3,k}$, $\tilde{\mathcal{C}}_{4,k}$, and the combination $\tilde{\mathcal{C}}_{6,k} + \tilde{\mathcal{C}}_{8,k}$ [representing the linearly dependent low-energy couplings $\tilde{\mathcal{C}}_{5,k}$, $\tilde{\mathcal{C}}_{6,k}$, and $\tilde{\mathcal{C}}_{8,k}$, cf. Eq. (23)] is thereby split into bosonic and fermionic loop contributions. The results exhibit a clear dominance of the fermionic quantum fluctuations as compared to the bosonic ones, astonishingly, even for relatively low energies below the scale of chiral-symmetry breaking (300–400 MeV and 400–500 MeV for $\Lambda_{UV} = 500$ MeV and $\Lambda_{UV} = 1$ GeV, respectively). This illustration nicely demonstrates the naturally emerging fluctuation hierarchy of quark loops at larger momenta and the pNGB fluctuations at low energy-momentum scales within the FRG. From the upcoming pNGB fluctuations and the onset of “flattening” in the fermionic curve in the rough region of 50 – 150 MeV (for both cutoff scenarios) we infer an appropriate transition scale from the

linear QMDM to its nonlinear low-energy limit of the same order, verifying the scales found in Refs. [2, 3].

The geometrical constants $\tilde{\mathcal{C}}_{1,k}$ and $\tilde{\mathcal{Z}}_{2,k}$ are not shown in Fig. 3, since their scaling behavior is essentially dictated by the pion decay constant and the pion wave-function renormalization, see Eqs. (22) and (23). This means that they are fixed by the constant-radius condition (19) on the five-sphere. The (scale-independent) explicit symmetry breaking parameter h_{ESB} in Eq. (22) is given in Table IV in the Appendix and we consistently find that $\tilde{\mathcal{M}}_{\Pi,k} = M_{\pi,k}$. As for the higher-derivative interactions within the linearly realized QMDM in Sec. III A, the IR values of the low-energy couplings in the nonlinear picture are discussed in Sec. III C.

The phenomenon of fermion dominance in these calculations is rather robust and was already observed in the SO(4)-symmetric QMM [2]. However, in this work and the present study within the QMDM, it comes up the question about the sensibility of the computed low-energy couplings in the IR limit w.r.t. changes in the UV cutoff.

C. Cutoff dependences

We qualitatively elucidate the UV-cutoff dependences of the linear higher-derivative and the nonlinear low-energy couplings with a rather simple setup, see Fig. 4. Besides the two UV cutoffs (and tuning scenarios) introduced above (for a first glimpse into truncation and cutoff effects), we define the intermediate scale Λ_C at which we add the higher-derivative couplings to the LPA' flow. The latter is initialized at Λ_{UV} as before. Thus the presented curves in Sec. III A and Sec. III B equal the case of $\Lambda_C \equiv \Lambda_{UV}$. In order to qualitatively “measure” the cutoff dependence, the scale Λ_C is successively lowered (in separate FRG runs) in steps of 100 MeV (down to 100 MeV as the lower bound).

This strategy is motivated by the fact that the LPA' flow is comparably “constant” w.r.t. the inclusion of the higher-derivative interactions, meaning that it is a reason-

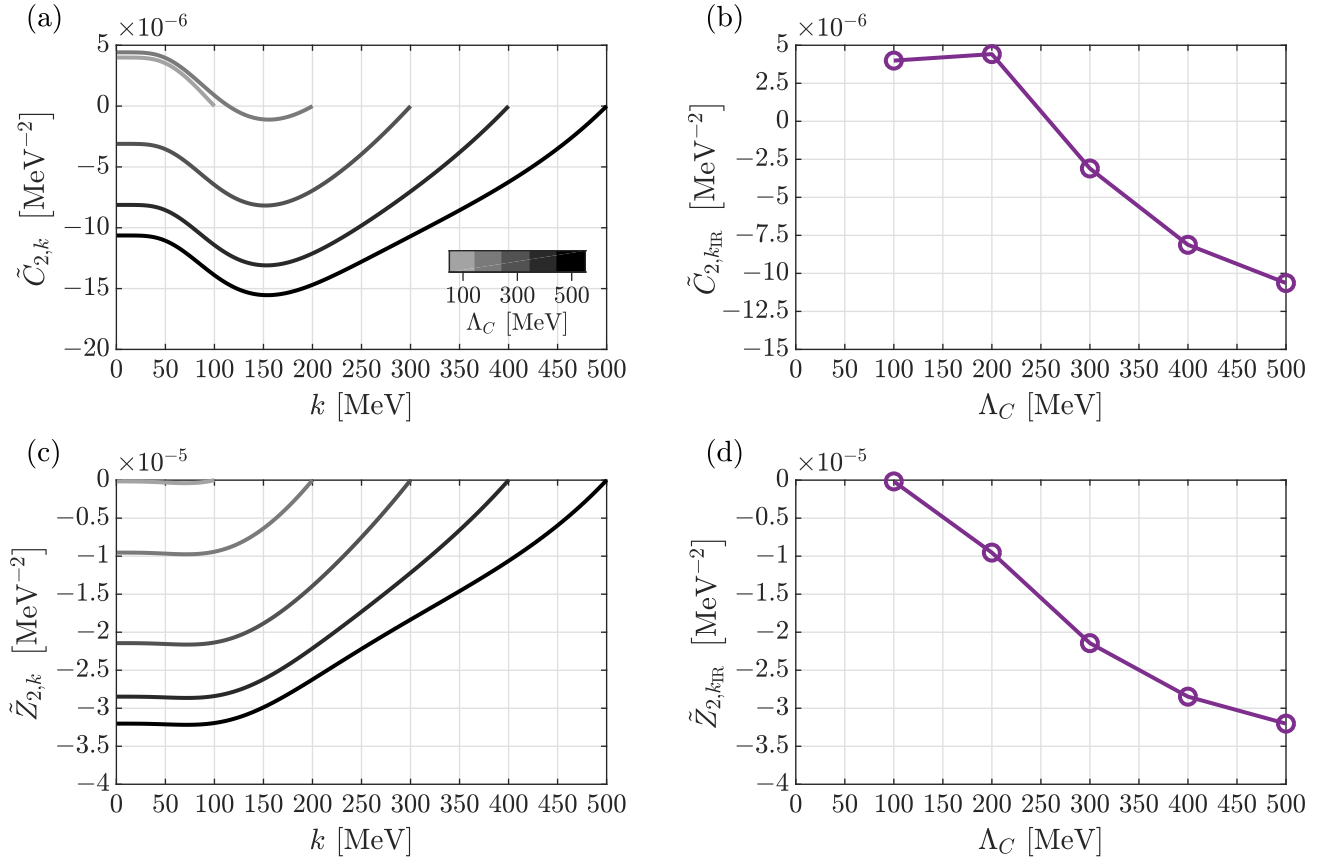


Figure 5. Scale evolution of the higher-derivative couplings $\tilde{C}_{2,k}$ and $\tilde{Z}_{2,k}$ as a function of the initialization scale Λ_C . The flow was tuned at $\Lambda_{\text{UV}} = 500$ MeV. The IR-limit values are shown in subfigures (b) and (d), respectively. The legend in subfigure (a) is valid for the panels (a) and (c).

able approximation to the “full” truncation (as concluded above) and that distorting alterations in other observables are minimized. In fact, the deviation between those truncations in terms of the IR masses of the pNGBs and the quarks is less than 1%, cf. again Table I [of course, one still has to consider the couplings of $\mathcal{O}(\partial^2)$ and $\mathcal{O}(\partial^4)$ to access the low-energy couplings of the model].

Tables II and III show the results of this procedure for the higher-derivative couplings (in the linear symmetry realization) and the low-energy couplings (in the nonlinear model), respectively. The IR values of the flows in Fig. 2 and Fig. 3 are listed in the second and seventh columns; it is immediate that the order of magnitude is cutoff-independent, while, at the same time, the difference between the cutoff scenarios is partly large [i.e., for the couplings of $\mathcal{O}(\partial^2)$ of the linear model]. However, the actually relevant couplings of $\mathcal{O}(\partial^4)$ of the linear model as well as all couplings of the respective nonlinear model only differ by less than 10%.

Concerning the variation of Λ_C , we plot the different FRG flows of the higher-derivative couplings of $\mathcal{O}(\partial^2)$ in a gray-scaled manner in Fig. 5 ($\Lambda_{\text{UV}} = 500$ MeV) and Fig. 6 ($\Lambda_{\text{UV}} = 1$ GeV). The black lines are identical to the respective curves in Fig. 2. The FRG flows are

further complemented by panels showing the IR values as a function of Λ_C (in addition to the complete set of IR values quoted again in Tables II and III). They reveal a persisting UV-cutoff dependence for larger Λ_C in the scenario of $\Lambda_{\text{UV}} = 500$ MeV [cf. Fig. 5(b) and Fig. 5(d)], but an almost “flat” curve for $\Lambda_{\text{UV}} = 1$ GeV [cf. Fig. 6(b) and Fig. 6(d)].

The first four rows in Table II underline the “robustness” of the LPA’ flow against the additional couplings of $\mathcal{O}(\partial^2)$ and $\mathcal{O}(\partial^4)$, underlying the variations of Λ_C . Solely the σ mass changes by more than 1%, when decreasing or increasing Λ_C (but still only by a maximum of around 5%); this justifies the setup of Fig. 4 a posteriori.

Analogously, the couplings of $\mathcal{O}(\partial^4)$ are presented in Fig. 7 and Fig. 8, directly given in form of the low-energy couplings according to Eq. (23). For the IR-limit values as a function of the scale Λ_C , we find the same behavior as for the $\mathcal{O}(\partial^2)$ -couplings, i.e., the curves and values only “converge” for the case that $\Lambda_{\text{UV}} = 1$ GeV. For initialization scales $\Lambda_C \gtrsim 800$ MeV, a reasonable settlement of the IR values of both the $\mathcal{O}(\partial^2)$ -couplings and those of $\mathcal{O}(\partial^4)$ sets in. This finding matches the scale proposed in Ref. [59] (in a similar thermodynamic consideration to en-

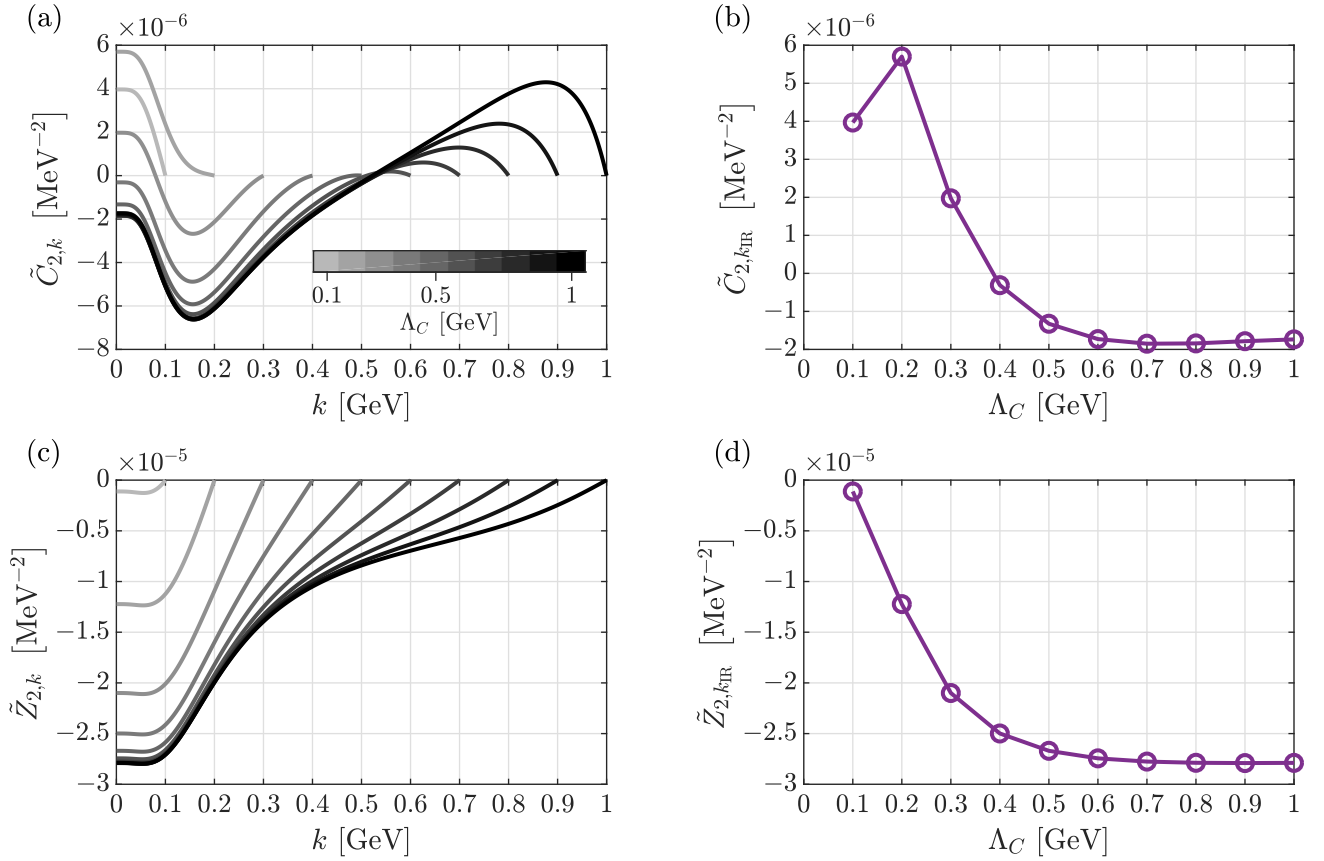


Figure 6. Scale evolution of the higher-derivative couplings $\tilde{C}_{2,k}$ and $\tilde{Z}_{2,k}$ as a function of the initialization scale Λ_C . The flow was tuned at $\Lambda_{\text{UV}} = 1$ GeV. The IR-limit values are shown in subfigures (b) and (d), respectively. The legend in subfigure (a) is valid for the panels (a) and (c).

sure UV-cut-off independence of the results). Let us stress that this scale has to be further constrained by the proper determination of the validity range of the QMDM from the dynamical-hadronization technique along the lines of Refs. [10, 19–24, 59, 70–72].

IV. SUMMARY AND OUTLOOK

The low-energy limit and qualitative features of the IR dynamics of the SO(6)-symmetric QMDM have been addressed within the FRG formalism. In order to determine the corresponding low-energy couplings, which have exclusively been generated from the FRG integration of quantum fluctuations, we considered a complete set of higher-derivative interactions beyond traditional approximation schemes (such as LPA and LPA' truncations) and transformed the linear effective action into a nonlinear pNGB model; the pNGB fields themselves act as coordinates on the vacuum manifold SO(6)/SO(5), which arises from the spontaneous breakdown of the chiral symmetry of QC₂D.

Consistent with recent studies in the SO(4)-symmetric QMM [1–3], we found the following main results:

- (a) The FRG flow of the low-energy couplings is heavily dominated by the quark fluctuations. The pNGB dynamics takes over below scales of 50 – 150 MeV, which naturally marks a fluctuation-induced transition (and renormalization) scale between the linear QMDM to its nonlinearly realized low-energy limit (i.e., the computed effective pNGB action).
- (b) The inclusion of higher-derivative interactions into the FRG flow demonstrates that LPA and LPA+Y truncations are rather insufficient, while its minimal extension (LPA') already takes major corrections into account.
- (c) The UV-cut-off independence of the fluctuation-generated low-energy couplings, as it was investigated in a simple qualitative manner, impose cutoff scales of $\Lambda_{\text{UV}} \gtrsim 800$ MeV. These scales are further constrained in the broader context of determining the validity range of the QMDM [which is expected to be below such scales [19–24, 59, 73] and highlights the complexity of finding appropriate cutoff scales]. Furthermore, it is questionable to what extent a “retuning” of the UV parameters at every scale Λ_C will change the results (albeit the effect

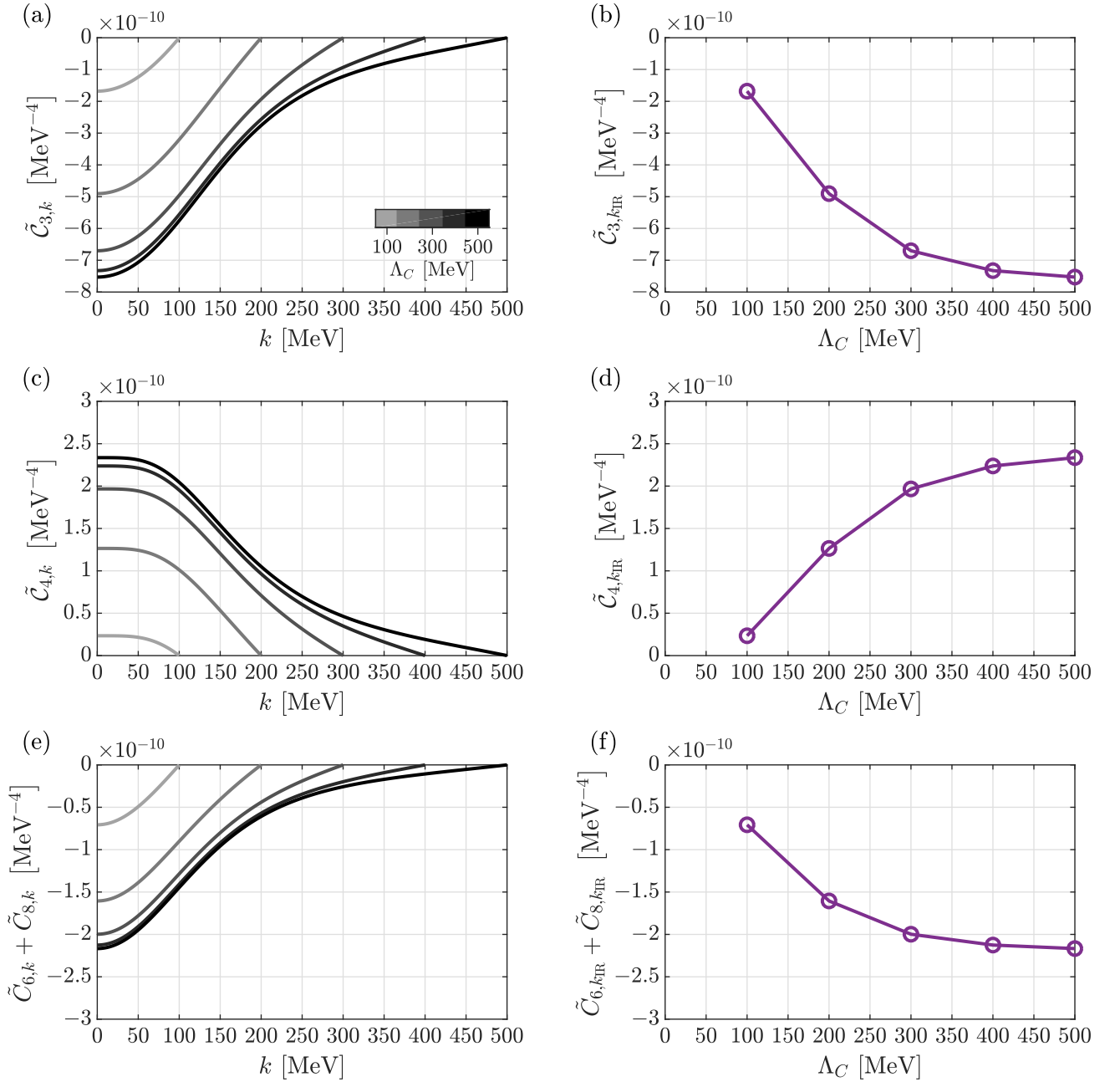


Figure 7. Scale evolution of the low-energy couplings $\tilde{C}_{3,k}$ and $\tilde{C}_{4,k}$, as well as the sum $\tilde{C}_{6,k} + \tilde{C}_{8,k}$ as a function of the initialization scale Λ_C . The flow was tuned at $\Lambda_{\text{UV}} = 500$ MeV. The IR-limit values are shown in subfigures (b), (d), and (f), respectively. The legend in subfigure (a) applies to the panels (a), (c), and (e).

of higher-derivative couplings is small, cf. Tables I and II).

This qualitative analysis is the basis for more involved investigations regarding the validity range of the QMDM and a smooth transition from fundamental to low-energy operators. Especially, result (c) and the fact that the higher-derivative interactions of $\mathcal{O}(\partial^2)$ experience large corrections close to the UV-cutoff scale raise the question about possible distortions by the usage of “corrupted” d.o.f. in the high-energy domain. This neces-

sitates a determination of the low-energy couplings from larger UV scales with the help of dynamical hadronization [10, 70–72] as well as a detailed discussion of cutoff (in)dependences in the generic sense of renormalization-group consistency [73]. Nevertheless, the presented study follows the ultimate goal of consistently generating low-energy couplings within the effective average action formalism, towards “FRG-improved” model calculations. It is understood as a complementary work to our recent studies within the SO(4)-invariant QMM.

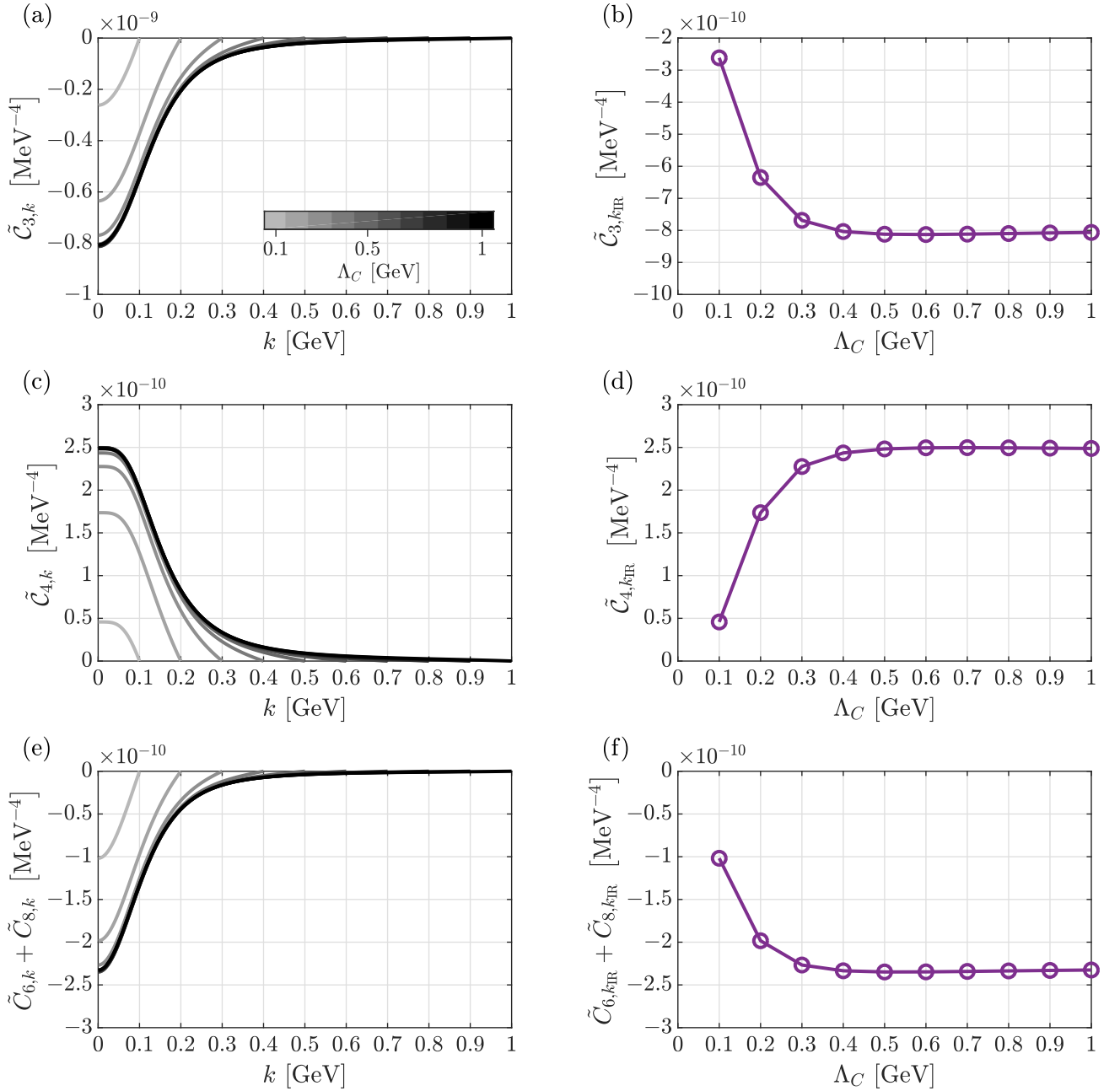


Figure 8. Scale evolution of the low-energy couplings $\tilde{C}_{3,k}$ and $\tilde{C}_{4,k}$, as well as the sum $\tilde{C}_{6,k} + \tilde{C}_{8,k}$ as a function of the initialization scale Λ_C . The flow was tuned at $\Lambda_{UV} = 1$ GeV. The IR-limit values are shown in subfigures (b), (d), and (f), respectively. The legend in subfigure (a) applies to the panels (a), (c), and (e).

Moreover, the effect of higher-derivative interactions should be studied at nonzero temperatures and densities. It would be interesting to learn how they change the picture in the (expectedly very diverse) large-density regime, as an extension (or addition) to Refs. [42, 55, 58, 59, 74]. Finally, the flow of the nonlinear effective pNGB action itself and the pion-mass dependence of the presented results will attract our attention in the near future.

ACKNOWLEDGMENTS

The authors thank Dennis D. Dietrich, Adrian Koenigstein, Mario Mitter, Jan M. Pawłowski, Dirk H. Rischke, Bernd-Jochen Schaefer, and Lorenz von Smekal for helpful discussions.

Appendix: Flow equations

We extract the flow equations of the scale-dependent quantities in the ansatz (7) from the Wetterich equation (6) via functional differentiation w.r.t. the corresponding

fields. The concrete expressions for the flows of the effective potential U_k , the Yukawa coupling y_k , the wavefunction renormalization factors Z_k^π , Z_k^σ , and Z_k^ψ , as well as the higher-derivative couplings $C_{2,k}$, $Z_{2,k}$, and $C_{i,k}$, $i = 3, \dots, 8$, read in a diagrammatic language as follows:

$$\partial_k U_k = \mathcal{V}^{-1} \partial_k \Gamma_k = \mathcal{V}^{-1} \left(\frac{1}{2} \text{diag}_\sigma + \frac{1}{2} \text{diag}_\pi + \frac{1}{2} \text{diag}_{\pi^4} + \frac{1}{2} \text{diag}_{\pi^5} - \text{diag}_\psi \right), \quad (\text{A.1})$$

$$\begin{aligned} \partial_k y_k &= -\frac{1}{4N_c N_f} \mathcal{V}^{-1} \frac{1}{\sigma} \text{tr} \left[\frac{\delta^2}{\delta \bar{\psi}(0) \delta \psi(0)} \partial_k \Gamma_k \right] \\ &= -\frac{1}{4N_c N_f} \mathcal{V}^{-1} \frac{1}{\sigma} \text{tr} \left(\frac{1}{2} \text{diag}_{\psi\sigma} + \frac{1}{2} \text{diag}_{\psi\pi} + \frac{1}{2} \text{diag}_{\psi\pi^4} \right. \\ &\quad \left. + \frac{1}{2} \text{diag}_{\psi\pi^5} - \text{diag}_{\psi\sigma} - \text{diag}_{\psi\pi} - \text{diag}_{\psi\pi^4} - \text{diag}_{\psi\pi^5} \right), \end{aligned} \quad (\text{A.2})$$

$$\begin{aligned} \partial_k Z_k^\pi &= \mathcal{V}^{-1} \frac{d}{dp^2} \Big|_{p^2=0} \frac{\delta^2 \partial_k \Gamma_k}{\delta \pi^1(-p) \delta \pi^1(p)} \\ &= \mathcal{V}^{-1} \frac{d}{dp^2} \Big|_{p^2=0} \left(\frac{1}{2} \text{diag}_{\pi\pi} + \frac{1}{2} \text{diag}_{\pi\sigma} - \text{diag}_{\psi\psi} \right. \\ &\quad \left. - \frac{1}{2} \text{diag}_{\sigma\sigma} - \frac{1}{2} \text{diag}_{\pi\pi} - \frac{1}{2} \text{diag}_{\pi^4\pi^4} - \frac{1}{2} \text{diag}_{\pi^5\pi^5} \right), \end{aligned} \quad (\text{A.3})$$

$$\begin{aligned} \partial_k Z_k^\sigma &= \mathcal{V}^{-1} \frac{d}{dp^2} \Big|_{p^2=0} \frac{\delta^2 \partial_k \Gamma_k}{\delta \sigma(-p) \delta \sigma(p)} \\ &= \mathcal{V}^{-1} \frac{d}{dp^2} \Big|_{p^2=0} \left(\frac{1}{2} \text{diag}_{\sigma\sigma} + \frac{1}{2} \text{diag}_{\sigma\pi} + \frac{1}{2} \text{diag}_{\sigma\pi^4} \right) \end{aligned}$$

$$\begin{aligned}
& + \frac{1}{2} \left(\begin{array}{c} \text{Diagram 1: } \sigma \text{ (left), } \pi^5 \text{ (top), } \pi^5 \text{ (right), } \sigma \text{ (right), } \pi^5 \text{ (bottom)} \\ \text{Diagram 2: } \psi \text{ (left), } \psi \text{ (top), } \psi \text{ (right), } \psi \text{ (right), } \psi \text{ (bottom)} \end{array} \right) \\
& - \frac{1}{2} \left(\begin{array}{c} \text{Diagram 3: } \sigma \text{ (left), } \sigma \text{ (right), } \sigma \text{ (right), } \sigma \text{ (right), } \sigma \text{ (bottom)} \\ \text{Diagram 4: } \pi \text{ (left), } \pi \text{ (top), } \pi \text{ (right), } \pi \text{ (right), } \pi \text{ (bottom)} \\ \text{Diagram 5: } \pi^4 \text{ (left), } \pi^4 \text{ (top), } \pi^4 \text{ (right), } \pi^4 \text{ (right), } \pi^4 \text{ (bottom)} \\ \text{Diagram 6: } \pi^5 \text{ (left), } \pi^5 \text{ (top), } \pi^5 \text{ (right), } \pi^5 \text{ (right), } \pi^5 \text{ (bottom)} \end{array} \right), \quad (\text{A.4})
\end{aligned}$$

$$\begin{aligned}
\partial_k Z_k^\psi &= -\frac{i}{4N_c N_f} \mathcal{V}^{-1} \frac{d}{dp^2} \Big|_{p^2=0} \text{tr} \left[\frac{\delta^2}{\delta\bar{\psi}(p)\delta\psi(p)} \partial_k \Gamma_k \gamma_\mu p_\mu \right] \\
&= -\frac{i}{4N_c N_f} \mathcal{V}^{-1} \frac{d}{dp^2} \Big|_{p^2=0} \text{tr} \left[\left(\begin{array}{c} \frac{1}{2} \left(\begin{array}{c} \text{Diagram 1: } \psi \text{ (left), } \sigma \text{ (top), } \sigma \text{ (right), } \psi \text{ (right), } \psi \text{ (bottom)} \\ \text{Diagram 2: } \psi \text{ (left), } \pi \text{ (top), } \pi \text{ (right), } \psi \text{ (right), } \psi \text{ (bottom)} \\ \text{Diagram 3: } \psi \text{ (left), } \pi^4 \text{ (top), } \pi^4 \text{ (right), } \psi \text{ (right), } \psi \text{ (bottom)} \end{array} \right) \right. \\
& \quad + \frac{1}{2} \left(\begin{array}{c} \text{Diagram 4: } \psi \text{ (left), } \pi^5 \text{ (top), } \pi^5 \text{ (right), } \psi \text{ (right), } \psi \text{ (bottom)} \\ \text{Diagram 5: } \psi \text{ (left), } \psi \text{ (top), } \psi \text{ (right), } \sigma \text{ (right), } \psi \text{ (bottom)} \\ \text{Diagram 6: } \psi \text{ (left), } \psi \text{ (top), } \psi \text{ (right), } \pi \text{ (right), } \psi \text{ (bottom)} \end{array} \right) \\
& \quad \left. - \left(\begin{array}{c} \text{Diagram 7: } \psi \text{ (left), } \psi \text{ (top), } \psi \text{ (right), } \pi^4 \text{ (right), } \psi \text{ (bottom)} \\ \text{Diagram 8: } \psi \text{ (left), } \psi \text{ (top), } \psi \text{ (right), } \pi^5 \text{ (right), } \psi \text{ (bottom)} \end{array} \right) \gamma_\mu p_\mu \right], \quad (\text{A.5})
\end{aligned}$$

$$\begin{aligned}
\partial_k C_{2,k} &= \frac{1}{2} \mathcal{V}^{-1} \frac{d}{dp^2} \Big|_{p^2=0} \frac{\delta^4 \partial_k \Gamma_k}{\delta\pi^1(p)\delta\pi^2(-p)\delta\pi^1(0)\delta\pi^2(0)} \\
&= \frac{1}{2} \mathcal{V}^{-1} \frac{d}{dp^2} \Big|_{p^2=0} \left(\begin{array}{c} -\frac{1}{2} \left(\begin{array}{c} \text{Diagram 1: } \pi \text{ (left), } \sigma \text{ (top), } \sigma \text{ (right), } \pi \text{ (right), } \pi \text{ (bottom)} \\ \text{Diagram 2: } \pi \text{ (left), } \pi \text{ (top), } \pi \text{ (right), } \sigma \text{ (right), } \pi \text{ (bottom)} \end{array} \right) + \frac{1}{2} \left(\begin{array}{c} \text{Diagram 3: } \pi \text{ (left), } \sigma \text{ (top), } \sigma \text{ (right), } \pi \text{ (right), } \pi \text{ (bottom)} \\ \text{Diagram 4: } \pi \text{ (left), } \pi \text{ (top), } \pi \text{ (right), } \pi \text{ (right), } \pi \text{ (bottom)} \end{array} \right) \\
& \quad + \frac{1}{2} \left(\begin{array}{c} \text{Diagram 5: } \pi \text{ (left), } \pi^4 \text{ (top), } \pi^4 \text{ (right), } \pi \text{ (right), } \pi \text{ (bottom)} \\ \text{Diagram 6: } \pi \text{ (left), } \pi^5 \text{ (top), } \pi^5 \text{ (right), } \pi \text{ (right), } \pi \text{ (bottom)} \end{array} \right) - \frac{1}{2} \left(\begin{array}{c} \text{Diagram 7: } \pi \text{ (left), } \sigma \text{ (top), } \sigma \text{ (right), } \pi \text{ (right), } \pi \text{ (bottom)} \\ \text{Diagram 8: } \pi \text{ (left), } \pi \text{ (top), } \pi \text{ (right), } \sigma \text{ (right), } \pi \text{ (bottom)} \end{array} \right) \\
& \quad - \frac{1}{2} \left(\begin{array}{c} \text{Diagram 9: } \pi \text{ (left), } \pi \text{ (top), } \pi \text{ (right), } \pi \text{ (right), } \pi \text{ (bottom)} \\ \text{Diagram 10: } \pi \text{ (left), } \sigma \text{ (top), } \sigma \text{ (right), } \pi \text{ (right), } \pi \text{ (bottom)} \\ \text{Diagram 11: } \pi \text{ (left), } \pi \text{ (top), } \pi \text{ (right), } \pi \text{ (right), } \pi \text{ (bottom)} \end{array} \right)
\end{array} \right)
\end{aligned}$$

$$+ \frac{1}{2} \left(\text{Diagram 1} + \frac{1}{2} \text{Diagram 2} - \text{Diagram 3} \right), \quad (\text{A.6})$$

$$\partial_k Z_{2,k} = \frac{1}{4} \mathcal{V}^{-1} \left. \frac{d}{dp^2} \right|_{p^2=0} \frac{\delta^4 \partial_k \Gamma_k}{\delta \pi^1(p) \delta \pi^2(0) \delta \pi^1(-p) \delta \pi^2(0)}, \quad (\text{A.7})$$

$$\partial_k C_{3,k} = \frac{5}{576} \left\{ \frac{208}{5} \partial_k C_{5,k} - 112 \partial_k C_{6,k} + 32 \partial_k C_{7,k} - \frac{224}{5} \partial_k C_{8,k} + \mathcal{V}^{-1} \left(\frac{\partial}{\partial p_{1,\mu}} \frac{\partial}{\partial p_{2,\mu}} \frac{\partial}{\partial p_{3,\nu}} \frac{\partial}{\partial p_{1,\nu}} \right. \right. \\ \left. \left. - \frac{7}{10} \frac{\partial}{\partial p_{1,\mu}} \frac{\partial}{\partial p_{2,\mu}} \frac{\partial}{\partial p_{3,\nu}} \frac{\partial}{\partial p_{2,\nu}} \right) \right|_{p_1=p_2=p_3=0} \frac{\delta^4 \partial_k \Gamma_k}{\delta \pi^1(p_1) \delta \pi^2(p_2) \delta \pi^1(p_3) \delta \pi^2(-p_1-p_2-p_3)} \Bigg\}, \quad (\text{A.8})$$

$$\partial_k C_{4,k} = -\frac{1}{288} \left\{ -16 \partial_k C_{5,k} - 400 \partial_k C_{6,k} + 32 \partial_k C_{7,k} - 160 \partial_k C_{8,k} + \mathcal{V}^{-1} \left(\frac{\partial}{\partial p_{1,\mu}} \frac{\partial}{\partial p_{2,\mu}} \frac{\partial}{\partial p_{3,\nu}} \frac{\partial}{\partial p_{1,\nu}} \right. \right. \\ \left. \left. - \frac{5}{2} \frac{\partial}{\partial p_{1,\mu}} \frac{\partial}{\partial p_{2,\mu}} \frac{\partial}{\partial p_{3,\nu}} \frac{\partial}{\partial p_{2,\nu}} \right) \right|_{p_1=p_2=p_3=0} \frac{\delta^4 \partial_k \Gamma_k}{\delta \pi^1(p_1) \delta \pi^2(p_2) \delta \pi^1(p_3) \delta \pi^2(-p_1-p_2-p_3)} \Bigg\}, \quad (\text{A.9})$$

$$\partial_k C_{5,k} = \frac{1}{96} \mathcal{V}^{-1} \left(\frac{\partial}{\partial p_{2,\mu}} \frac{\partial}{\partial p_{2,\mu}} \frac{\partial}{\partial p_{2,\nu}} \frac{\partial}{\partial p_{3,\nu}} \right. \\ \left. - \frac{1}{2} \frac{\partial}{\partial p_{2,\mu}} \frac{\partial}{\partial p_{2,\mu}} \frac{\partial}{\partial p_{2,\nu}} \frac{\partial}{\partial p_{2,\nu}} \right) \Big|_{p_2=p_3=0} \frac{\delta^4 \partial_k \Gamma_k}{\delta \pi^1(-p_2-p_3) \delta \pi^2(p_2) \delta \pi^1(p_3) \delta \pi^2(0)}, \quad (\text{A.10})$$

$$\partial_k C_{6,k} = -\frac{1}{96} \left\{ 160 \partial_k C_{5,k} + 64 \partial_k C_{7,k} + \mathcal{V}^{-1} \frac{\partial}{\partial p_{2,\mu}} \frac{\partial}{\partial p_{4,\mu}} \frac{\partial}{\partial p_{2,\nu}} \frac{\partial}{\partial p_{4,\nu}} \right|_{p_2=p_4=0} \frac{\delta^4 \partial_k \Gamma_k}{\delta \pi^1(-p_2-p_4) \delta \pi^2(p_2) \delta \pi^1(0) \delta \pi^2(p_4)} \\ \left. - \frac{1}{12} \mathcal{V}^{-1} \frac{\partial}{\partial p_\mu} \frac{\partial}{\partial p_\mu} \frac{\partial}{\partial p_\nu} \frac{\partial}{\partial p_\nu} \right|_{p=0} \frac{\delta^4 \partial_k \Gamma_k}{\delta \pi^1(-p) \delta \pi^2(0) \delta \pi^1(p) \delta \pi^2(0)} \Bigg\}, \quad (\text{A.11})$$

$$\partial_k C_{7,k} = -\frac{1}{384} \mathcal{V}^{-1} \frac{\partial}{\partial p_\mu} \frac{\partial}{\partial p_\mu} \frac{\partial}{\partial p_\nu} \frac{\partial}{\partial p_\nu} \Big|_{p=0} \frac{\delta^4 \partial_k \Gamma_k}{\delta \pi^1(-p) \delta \pi^2(p) \delta \pi^1(0) \delta \pi^2(0)}, \quad (\text{A.12})$$

$$\partial_k C_{8,k} = \frac{1}{96} \left\{ 160 \partial_k C_{5,k} + 64 \partial_k C_{7,k} + \mathcal{V}^{-1} \frac{\partial}{\partial p_{2,\mu}} \frac{\partial}{\partial p_{4,\mu}} \frac{\partial}{\partial p_{2,\nu}} \frac{\partial}{\partial p_{4,\nu}} \right|_{p_2=p_4=0} \frac{\delta^4 \partial_k \Gamma_k}{\delta \pi^1(-p_2-p_4) \delta \pi^2(p_2) \delta \pi^1(0) \delta \pi^2(p_4)} \\ \left. - \frac{5}{24} \mathcal{V}^{-1} \frac{\partial}{\partial p_\mu} \frac{\partial}{\partial p_\mu} \frac{\partial}{\partial p_\nu} \frac{\partial}{\partial p_\nu} \right|_{p=0} \frac{\delta^4 \partial_k \Gamma_k}{\delta \pi^1(-p) \delta \pi^2(0) \delta \pi^1(p) \delta \pi^2(0)} \Bigg\}, \quad (\text{A.13})$$

where the propagator $(\Gamma_k^{(2)} + R_k)^{-1}$ is represented by a (solid or dashed) line (depending on its bosonic or fermionic character) and the supertrace obviously translates into a closed loop. The regulator insertion $\partial_k R_k$ is denoted by a “crossed” circle at the top of the loops. Moreover, the functional derivatives generate external legs, such that the flow involves two-point and even four-point functions, and each diagram on the right-hand side includes all possible permutations of them. These legs come with the momentum p or p_i , $i \in \{1, 2, 3, 4\}$, and the factor \mathcal{V} is the (infinite) space-time volume. Five and six-point vertices stemming from the effective potential are truncated. Finally, the different d.o.f. are depicted using the following colors: $\sigma \rightarrow$ blue, $\vec{\pi} \rightarrow$ red, $\pi^4 \rightarrow$ orange, $\pi^5 \rightarrow$ violet, and $\psi \rightarrow$ black; this is further true for the regulator insertions.

From Eq. (A.7) on, we omitted the diagrams for reasons of clarity [for all pion four-point functions, the diagrams are the same as in Eq. (A.6)]. Note also that we have only given one single equation for the pNGB wave-function renormalization Z_k^π (i.e., the one of the “ordinary” pions), since all of them are degenerate due to the symmetry of the QMDM in vacuum. The analytic expressions of the flow equations are obtained by using the *Mathematica* packages *FeynCalc* [75–77], *DoFun* [78, 79], and *FormTracer* [80].

To solve the FRG flow equations, the effective potential U_k is approximated by the Taylor polynomial

$$U_k(\rho) = \sum_{n=1}^N \frac{\alpha_{n,k}}{n!} (\rho - \chi)^n, \quad (\text{A.14})$$

with the k -independent expansion point χ . The choice of $N = 6$ has proven to be numerically stable [81]. The Taylor coefficients $\alpha_{n,k}$, $n = 1, \dots, 6$, are computed from Eq. (A.1) as

$$\partial_k \alpha_{n,k} = \left. \frac{\partial^n}{\partial \rho^n} \right|_{\chi} \partial_k U_k. \quad (\text{A.15})$$

The second coefficient $\alpha_{2,k}$ coincides (up to a factor of minus one-half) with the momentum-independent quartic interaction as mentioned in Sec. II and Sec. III,

$$C_{1,k} = -\frac{\alpha_{2,k}}{2}. \quad (\text{A.16})$$

All other variables are also evaluated at the point $\rho = \chi$, which is chosen to be slightly larger than the IR minimum of U_k . The initialization values of the FRG flow for the two different UV-cutoff scenarios discussed in Sec. III are summarized in Table IV. We emphasize once more that the higher-derivative couplings $C_{2,k}$, $Z_{2,k}$, and $C_{i,k}$, $i = 3, \dots, 8$, start at zero in the UV and are therefore solely generated from quantum fluctuations during the FRG integration process.

For the numerical integration, we employ exponential-

type regulators,

$$\begin{aligned} R_k^\pi(q^2) &= Z_k^\pi q^2 r\left(\frac{q^2}{k^2}\right), \\ R_k^\sigma(q^2) &= Z_k^\sigma q^2 r\left(\frac{q^2}{k^2}\right), \\ R_k^\psi(q) &= -i Z_k^\psi \gamma_\mu q_\mu r\left(\frac{q^2}{k^2}\right), \end{aligned} \quad (\text{A.17})$$

with the “shape function”

$$r(x) = \frac{1}{\exp(x) - 1}. \quad (\text{A.18})$$

As functions of the FRG scale k and the momentum q , the regulators (A.17) obey the limits

$$\begin{aligned} R_k &\rightarrow 0 \quad \text{for } k \rightarrow 0, \\ R_k &\rightarrow \infty \quad \text{for } k \rightarrow \Lambda_{\text{UV}} \rightarrow \infty, \\ R_k &> 0 \quad \text{for } q \rightarrow 0, \\ R_k &\rightarrow 0 \quad \text{for } q \rightarrow \infty. \end{aligned} \quad (\text{A.19})$$

For the sake of completeness, we discuss the scaling behavior of the (renormalized) Taylor coefficients, $\tilde{\alpha}_{n,k} \equiv \alpha_{n,k}/(Z_k^\pi)^n$, $n = 1, \dots, 6$, the Yukawa coupling \tilde{y}_k , and the wave-function renormalization factors Z_k^π , Z_k^σ , and Z_k^ψ in this Appendix: The Taylor coefficients (in dimensionless form) are plotted in Fig. 9 ($\Lambda_{\text{UV}} = 500$ MeV) and Fig. 10 ($\Lambda_{\text{UV}} = 1$ GeV). These flows determine the masses and the decay constants, which are shown in Fig. 1 in Sec. III. They exhibit strong corrections from the LPA and LPA+Y truncations towards the “higher” ones, as it has been documented above. However, the LPA’ approximation is already close to the truncations including higher-derivative interactions, $\mathcal{O}(\partial^2)$ and $\mathcal{O}(\partial^4)$. The values of the (renormalized) coefficients are quoted in Table I in Sec. III.

Similarly to Fig. 1 in Sec. III as well as Fig. 9 and Fig. 10, Fig. 11 underlines the importance of the corrections from the wave-function renormalization, as compared to

Table IV. UV parameters.

Parameter	$\Lambda_{\text{UV}} = 500 \text{ MeV}$	$\Lambda_{\text{UV}} = 1 \text{ GeV}$
χ	$(53.03 \text{ MeV})^2$	$(32.30 \text{ MeV})^2$
$\alpha_{1,\Lambda_{\text{UV}}}$	$(514 \text{ MeV})^2$	$(1080 \text{ MeV})^2$
$\alpha_{2,\Lambda_{\text{UV}}}$	1	243
$\alpha_{n,\Lambda_{\text{UV}}}$ $\{n > 2\}$	0	0
h_{ESB}	$2.155 \times 10^6 \text{ MeV}^3$	$3.635 \times 10^6 \text{ MeV}^3$
$y_{\Lambda_{\text{UV}}}$	4.5	5.0
$Z_{\Lambda_{\text{UV}}}^{\pi,\sigma,\psi}$	1	1
$C_{i,\Lambda_{\text{UV}}}$, $i \in \{2, \dots, 8\}$	0	0
$Z_{2,\Lambda_{\text{UV}}}$	0	0

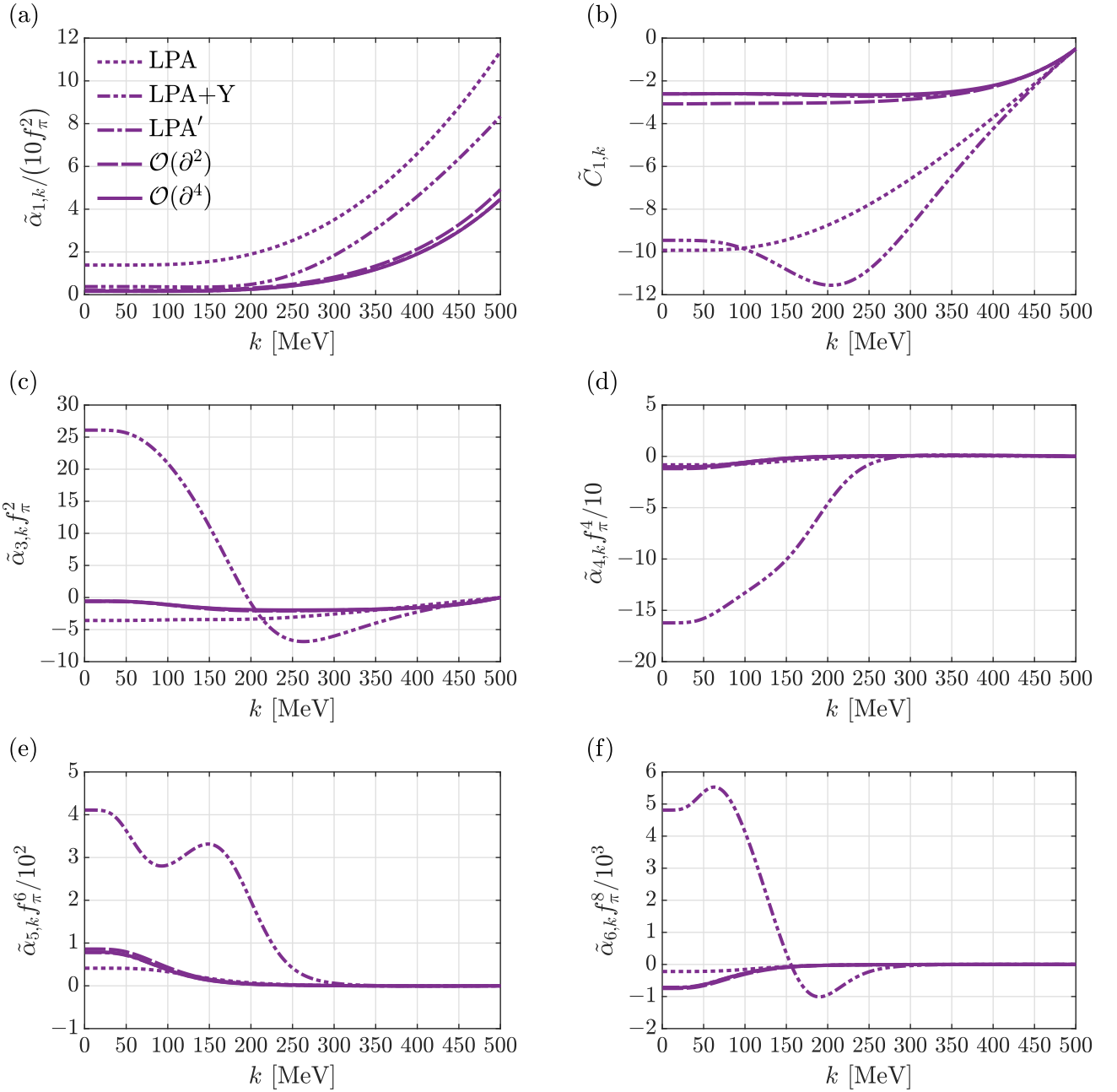


Figure 9. FRG flows of the (renormalized) Taylor coefficients ($\Lambda_{\text{UV}} = 500$ MeV). The legend of subfigure (a) applies to all panels.

the (crudest) truncation LPA+Y. Within the latter, the value of γ_k increases in total to its IR-limit value, while it decreases in “higher” truncations, cf. Fig. 11(a) and Table I. This difference is even more drastic for the scenario with a larger UV cutoff shown in Fig. 11(b) and we end up with a quite “mild” flow of the parameter $\tilde{\gamma}_k$, see also Ref. [59] for very similar results.

Starting from their initialization at one, the bosonic wave-function renormalization factors Z_k^π and Z_k^σ increase during the flow. This behavior is shown in Fig. 12. Especially, the extra growth of the Z_k^σ -parameter below

roughly 150 MeV is ascribed to the pure pion loops exclusively occurring in Eq. (A.4) [and not in Eq. (A.3)]. This scale matches the decoupling of the quark fields from the FRG flow, as it is depicted in Fig. 3. Interestingly, the findings for the wave-function renormalization in the LPA' approximation are closest to the “full” result of $\mathcal{O}(\partial^4)$. This phenomenon is inherited to many other couplings and coefficients, see once again Table I. Finally, there is basically no significant difference between the various truncations for the scale evolution of the fermionic wave-function renormalization Z_k^ψ .

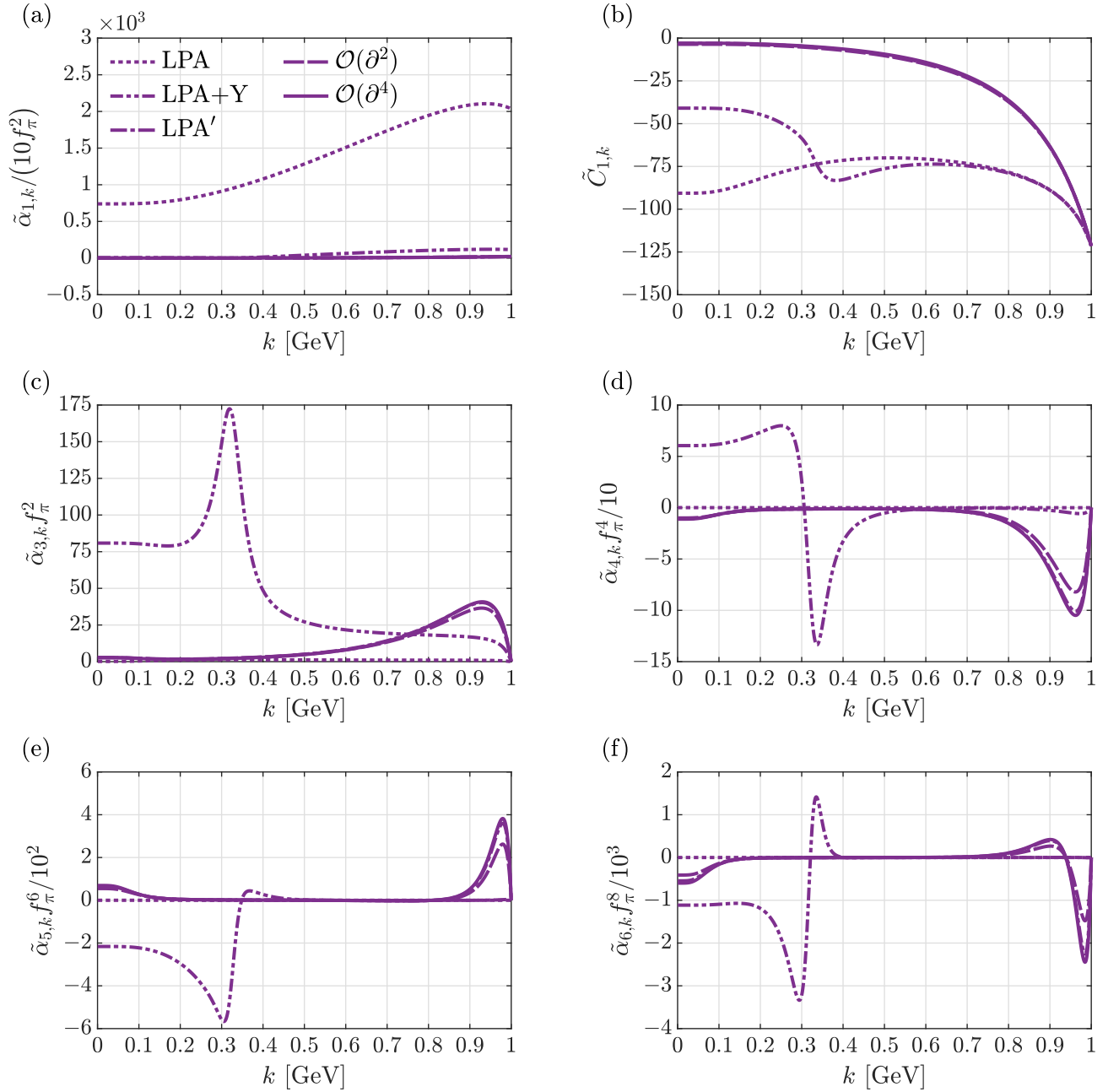


Figure 10. FRG flows of the (renormalized) Taylor coefficients ($\Lambda_{UV} = 1$ GeV). The legend of subfigure (a) applies to all panels.

-
- [1] J. Eser, F. Divotgey, M. Mitter, and D. H. Rischke, Phys. Rev. **D98**, 014024 (2018), arXiv:1804.01787 [hep-ph].
- [2] F. Divotgey, J. Eser, and M. Mitter, Phys. Rev. **D99**, 054023 (2019), arXiv:1901.02472 [hep-ph].
- [3] J. Eser, F. Divotgey, and M. Mitter, *Proceedings, 9th International Workshop on Chiral Dynamics (CD18): Durham (NC), United States*, PoS **CD2018**, 060 (2019), arXiv:1902.04804 [hep-ph].
- [4] C. Wetterich, Phys. Lett. **B301**, 90 (1993).
- [5] M. Bonini, M. D’Attanasio, and G. Marchesini, Nucl. Phys. **B409**, 441 (1993), arXiv:hep-th/9301114 [hep-th].
- [6] U. Ellwanger, *Proceedings, Workshop on Quantum field theoretical aspects of high energy physics: Bad Frankenhausen, Germany, September 20-24, 1993*, Z. Phys. **C62**, 503 (1994), [,206(1993)],

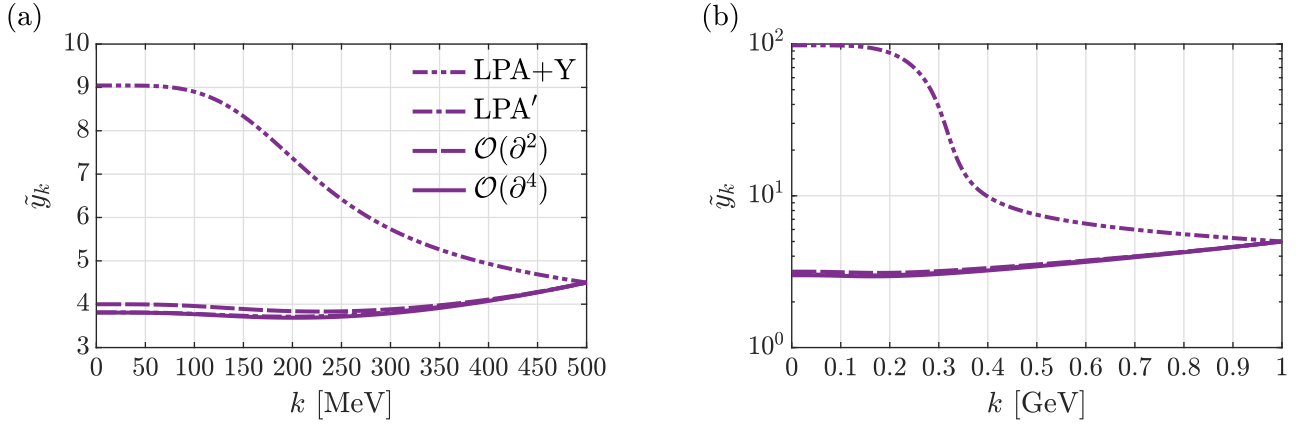


Figure 11. FRG flow of the (renormalized) Yukawa coupling \hat{y}_k . The legend in subfigure (a) is also valid for subfigure (b).

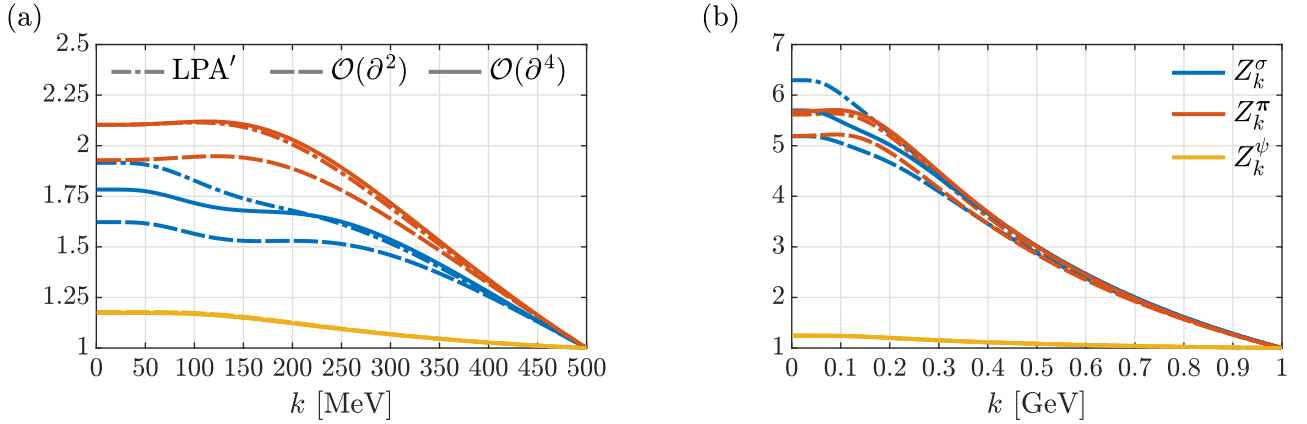


Figure 12. Scale evolution of the bosonic and fermionic wave-function renormalization factors Z_k^π , Z_k^σ , and Z_k^ψ . The legends in subfigures (a) and (b) apply to all panels.

- arXiv:hep-ph/9308260 [hep-ph].
- [7] T. R. Morris, Int. J. Mod. Phys. **A9**, 2411 (1994), arXiv:hep-ph/9308265 [hep-ph].
- [8] J. Berges, N. Tetradis, and C. Wetterich, Phys. Rept. **363**, 223 (2002), arXiv:hep-ph/0005122 [hep-ph].
- [9] C. Bagnuls and C. Bervillier, Phys. Rept. **348**, 91 (2001), arXiv:hep-th/0002034 [hep-th].
- [10] J. M. Pawłowski, Annals Phys. **322**, 2831 (2007), arXiv:hep-th/0512261 [hep-th].
- [11] N. Dupuis, L. Canet, A. Eichhorn, W. Metzner, J. Pawłowski, M. Tissier, and N. Wschebor, (2020), arXiv:2006.04853 [cond-mat.stat-mech].
- [12] F. Gürsey, Nuovo Cim. **16**, 230 (1960).
- [13] M. Gell-Mann and M. Lévy, Nuovo Cim. **16**, 705 (1960).
- [14] J. S. Schwinger, Phys. Lett. **24B**, 473 (1967).
- [15] S. Weinberg, Phys. Rev. **166**, 1568 (1968).
- [16] C. G. Callan, Jr., S. R. Coleman, J. Wess, and B. Zumino, Phys. Rev. **177**, 2247 (1969).
- [17] S. R. Coleman, J. Wess, and B. Zumino, Phys. Rev. **177**, 2239 (1969).
- [18] K. Meetz, J. Math. Phys. **10**, 589 (1969).
- [19] J. Braun, L. Fister, J. M. Pawłowski, and F. Rennecke, Phys. Rev. **D94**, 034016 (2016), arXiv:1412.1045 [hep-ph].
- [20] M. Mitter, J. M. Pawłowski, and N. Strodthoff, Phys. Rev. **D91**, 054035 (2015), arXiv:1411.7978 [hep-ph].
- [21] A. K. Cyrol, M. Mitter, J. M. Pawłowski, and N. Strodthoff, Phys. Rev. **D97**, 054006 (2018), arXiv:1706.06326 [hep-ph].
- [22] J. París-López, R. Alkofer, A. Maas, W. Mian, M. Mitter, J. Pawłowski, and H. Sanchis-Alepuz, *Proceedings, 5th FAIR NExt generation ScientistS (FAIRNESS 2017): Sitges, Barcelona, Spain, May 28-June 3, 2018*, J. Phys. Conf. Ser. **1024**, 012009 (2018).
- [23] R. Alkofer, A. Maas, W. A. Mian, M. Mitter, J. París-López, J. M. Pawłowski, and N. Wink, Phys. Rev. D **99**, 054029 (2019), arXiv:1810.07955 [hep-ph].
- [24] W.-j. Fu, J. M. Pawłowski, and F. Rennecke, Phys. Rev. D **101**, 054032 (2020), arXiv:1909.02991 [hep-ph].
- [25] A. Nakamura, Phys. Lett. B **149**, 391 (1984).
- [26] S. Hands, J. B. Kogut, M.-P. Lombardo, and S. E. Morrison, Nucl. Phys. B **558**, 327 (1999), arXiv:hep-lat/9902034.
- [27] S. Hands, I. Montvay, S. Morrison, M. Oevers, L. Scorzato, and J. Skullerud, Eur. Phys. J. C **17**, 285 (2000), arXiv:hep-lat/0006018.

- [28] S. Hands, I. Montvay, L. Scorzato, and J. Skullerud, *Eur. Phys. J. C* **22**, 451 (2001), arXiv:hep-lat/0109029.
- [29] S. Chandrasekharan and F.-J. Jiang, *Phys. Rev. D* **74**, 014506 (2006), arXiv:hep-lat/0602031.
- [30] S. Hands, S. Kim, and J.-I. Skullerud, *Eur. Phys. J. C* **48**, 193 (2006), arXiv:hep-lat/0604004.
- [31] S. Hands, P. Kenny, S. Kim, and J.-I. Skullerud, *Eur. Phys. J. A* **47**, 60 (2011), arXiv:1101.4961 [hep-lat].
- [32] S. Hands, S. Kim, and J.-I. Skullerud, *Phys. Lett. B* **711**, 199 (2012), arXiv:1202.4353 [hep-lat].
- [33] S. Cotter, P. Giudice, S. Hands, and J.-I. Skullerud, *Phys. Rev. D* **87**, 034507 (2013), arXiv:1210.4496 [hep-lat].
- [34] T. Boz, S. Cotter, L. Fister, D. Mehta, and J.-I. Skullerud, *Eur. Phys. J. A* **49**, 87 (2013), arXiv:1303.3223 [hep-lat].
- [35] P. Scior and L. von Smekal, *Phys. Rev. D* **92**, 094504 (2015), arXiv:1508.00431 [hep-lat].
- [36] J. Wilhelm, L. Holicki, D. Smith, B. Wellegehausen, and L. von Smekal, *Phys. Rev. D* **100**, 114507 (2019), arXiv:1910.04495 [hep-lat].
- [37] T. Boz, P. Giudice, S. Hands, and J.-I. Skullerud, *Phys. Rev. D* **101**, 074506 (2020), arXiv:1912.10975 [hep-lat].
- [38] V. Bornyakov, V. Braguta, A. Nikolaev, and R. Rogalyov, (2020), arXiv:2003.00232 [hep-lat].
- [39] J. Kogut, M. A. Stephanov, and D. Toublan, *Phys. Lett. B* **464**, 183 (1999), arXiv:hep-ph/9906346.
- [40] L. Kondratyuk, M. Giannini, and M. Krivoruchenko, *Phys. Lett. B* **269**, 139 (1991).
- [41] R. Rapp, T. Schäfer, E. V. Shuryak, and M. Velkovsky, *Phys. Rev. Lett.* **81**, 53 (1998), arXiv:hep-ph/9711396.
- [42] J. Kogut, M. A. Stephanov, D. Toublan, J. Verbaarschot, and A. Zhitnitsky, *Nucl. Phys. B* **582**, 477 (2000), arXiv:hep-ph/0001171.
- [43] K. Splittorff, D. Son, and M. A. Stephanov, *Phys. Rev. D* **64**, 016003 (2001), arXiv:hep-ph/0012274.
- [44] K. Splittorff, D. Toublan, and J. Verbaarschot, *Nucl. Phys. B* **639**, 524 (2002), arXiv:hep-ph/0204076.
- [45] G. V. Dunne and S. M. Nishigaki, *Nucl. Phys. B* **654**, 445 (2003), arXiv:hep-ph/0210219.
- [46] G. V. Dunne and S. M. Nishigaki, *Nucl. Phys. B* **670**, 307 (2003), arXiv:hep-ph/0306220.
- [47] C. Ratti and W. Weise, *Phys. Rev. D* **70**, 054013 (2004), arXiv:hep-ph/0406159.
- [48] T. Brauner, *Mod. Phys. Lett. A* **21**, 559 (2006), arXiv:hep-ph/0601010.
- [49] G.-f. Sun, L. He, and P. Zhuang, *Phys. Rev. D* **75**, 096004 (2007), arXiv:hep-ph/0703159.
- [50] T. Brauner, K. Fukushima, and Y. Hidaka, *Phys. Rev. D* **80**, 074035 (2009), [Erratum: *Phys. Rev. D* **81**, 119904 (2010)], arXiv:0907.4905 [hep-ph].
- [51] T. Kanazawa, T. Wettig, and N. Yamamoto, *JHEP* **08**, 003 (2009), arXiv:0906.3579 [hep-ph].
- [52] T. Kanazawa, T. Wettig, and N. Yamamoto, *Phys. Rev. D* **81**, 081701 (2010), arXiv:0912.4999 [hep-ph].
- [53] J. O. Andersen and T. Brauner, *Phys. Rev. D* **81**, 096004 (2010), arXiv:1001.5168 [hep-ph].
- [54] T. Zhang, T. Brauner, and D. H. Rischke, *JHEP* **06**, 064 (2010), arXiv:1005.2928 [hep-ph].
- [55] N. Strodthoff, B.-J. Schaefer, and L. von Smekal, *Phys. Rev. D* **85**, 074007 (2012), arXiv:1112.5401 [hep-ph].
- [56] S. Imai, H. Toki, and W. Weise, *Nucl. Phys. A* **913**, 71 (2013), arXiv:1210.1307 [nucl-th].
- [57] L. von Smekal, *Physics at all scales: The Renormalization Group. Proceedings, 49. Internationale Universitätswochen für Theoretische Physik, Winter School: Schladming, Austria, February 26-March 5, 2011*, *Nucl. Phys. Proc. Suppl.* **228**, 179 (2012), arXiv:1205.4205 [hep-ph].
- [58] N. Strodthoff and L. von Smekal, *Phys. Lett. B* **731**, 350 (2014), arXiv:1306.2897 [hep-ph].
- [59] N. Khan, J. M. Pawłowski, F. Rennecke, and M. M. Scherer, (2015), arXiv:1512.03673 [hep-ph].
- [60] R. Contant and M. Q. Huber, *Phys. Rev. D* **101**, 014016 (2020), arXiv:1909.12796 [hep-ph].
- [61] W. Pauli, *Nuovo Cim.* **6**, 204 (1957).
- [62] F. Gürsey, *Nuovo Cim.* **7**, 411 (1958).
- [63] K. G. Wilson, *Phys. Rev.* **D3**, 1818 (1971).
- [64] K. G. Wilson, *Phys. Rev.* **B4**, 3174 (1971).
- [65] K. G. Wilson, *Phys. Rev.* **B4**, 3184 (1971).
- [66] G. De Polsi, I. Balog, M. Tissier, and N. Wschebor, *Phys. Rev. E* **101**, 042113 (2020), arXiv:2001.07525 [cond-mat.stat-mech].
- [67] R. Percacci and O. Zanusso, *Phys. Rev.* **D81**, 065012 (2010), arXiv:0910.0851 [hep-th].
- [68] R. Flore, A. Wipf, and O. Zanusso, *Phys. Rev.* **D87**, 065019 (2013), arXiv:1207.4499 [hep-th].
- [69] M. Tanabashi *et al.* (Particle Data Group), *Phys. Rev.* **D98**, 030001 (2018).
- [70] H. Gies and C. Wetterich, *Phys. Rev.* **D65**, 065001 (2002), arXiv:hep-th/0107221 [hep-th].
- [71] H. Gies and C. Wetterich, *Phys. Rev.* **D69**, 025001 (2004), arXiv:hep-th/0209183 [hep-th].
- [72] S. Floerchinger and C. Wetterich, *Phys. Lett.* **B680**, 371 (2009), arXiv:0905.0915 [hep-th].
- [73] J. Braun, M. Leonhardt, and J. M. Pawłowski, *SciPost Phys.* **6**, 056 (2019), arXiv:1806.04432 [hep-ph].
- [74] M. Leonhardt, M. Pospiech, B. Schallmo, J. Braun, C. Drischler, K. Hebel, and A. Schwenk, (2019), arXiv:1907.05814 [nucl-th].
- [75] R. Mertig, M. Böhm, and A. Denner, *Comput. Phys. Commun.* **64**, 345 (1991).
- [76] V. Shtabovenko, R. Mertig, and F. Orellana, *Comput. Phys. Commun.* **207**, 432 (2016), arXiv:1601.01167 [hep-ph].
- [77] V. Shtabovenko, R. Mertig, and F. Orellana, (2020), arXiv:2001.04407 [hep-ph].
- [78] M. Q. Huber and J. Braun, *Comput. Phys. Commun.* **183**, 1290 (2012), arXiv:1102.5307 [hep-th].
- [79] M. Q. Huber, A. K. Cyrol, and J. M. Pawłowski, *Comput. Phys. Commun.* **248**, 107058 (2020), arXiv:1908.02760 [hep-ph].
- [80] A. K. Cyrol, M. Mitter, and N. Strodthoff,

Comput. Phys. Commun. **219**, 346 (2017),
arXiv:1610.09331 [hep-ph].
[81] J. M. Pawlowski and F. Ren-

necke, Phys. Rev. **D90**, 076002 (2014),
arXiv:1403.1179 [hep-ph].